Intratumoral delivery of engineered recombinant modified vaccinia virus Ankara expressing Flt3L and OX40L generates potent antitumor immunity through activating the cGAS/STING pathway and depleting tumor-infiltrating regulatory T cells

Ning Yang[1#], Yi Wang[1#], Shuaitong Liu[1], Joseph M. Luna[3], Gregory Mazo[1], Adrian Y. Tan[4], Tuo Zhang[4], Jiahu Wang[5], Wei Yan[6], John Choi[6], Anthony Rossi[1,2], Jenny Zhaoying Xiang[4], Charles M. Rice[3], Taha Merghoub[2,7,8], Jedd D. Wolchok[2,7,8], and Liang Deng[1,2,8]*

[1]Dermatology Service, Department of Medicine, Memorial Sloan Kettering Cancer Center, New York, NY 10065, USA.

[2]Weill Cornell Medical College, New York, NY 10065

[3]The Laboratory of Virology and Infectious Disease, The Rockefeller University, New York, NY, 10065, USA.

[4]Genomic Resources Core Facility, Weill Cornell Medical College, New York, NY, 10065, USA

[5]Genvira Biosciences, Ottawa, ON K1V 1C1, Canada

[6]IMVAQ Therapeutics, Sammamish, WA, 98021, USA

[7]Immuno-oncology service, Human Oncology and Pathogenesis Program; Memorial Sloan Kettering Cancer Center, New York, NY 10065, USA

[8]Parker Institute for Cancer Immunotherapy, Memorial Sloan Kettering Cancer Center, New York, NY, USA

*corresponding author. Mailing address for Liang Deng: Dermatology Service, Department of Medicine, Memorial Sloan Kettering Cancer Center, 1275 York Ave., New York, NY 10065. Email: dengl@mskcc.org. # These two authors contributed equally to this work.

One Sentence Summary: Intratumoral delivery of recombinant MVA for cancer immunotherapy

Summary

Intratumoral (IT) delivery of immune-activating viruses can serve as an important strategy to turn "cold" tumors into "hot" tumors, resulting in overcoming resistance to immune checkpoint blockade (ICB). Modified vaccinia virus Ankara (MVA) is a highly attenuated, non-replicative vaccinia virus that has a long history of human use. Here we report that IT recombinant MVA (rMVA), lacking E5R encoding an inhibitor of the DNA sensor cyclic GMP-AMP synthase (cGAS), expressing a dendritic cell growth factor, Fms-like tyrosine kinase 3 ligand (Flt3L), and a T cell co-stimulator, OX40L, generates strong antitumor immunity, which is dependent on $CD8^+$ T cells, the cGAS/STING-mediated cytosolic DNA-sensing pathway, and STAT1/STAT2-mediated type I IFN signaling. Remarkably, IT rMVA depletes $OX40^{hi}$ regulatory T cells via OX40L/OX40 interaction and IFNAR signaling. Taken together, our study provides a proof-of-concept for improving MVA-based cancer immunotherapy, through modulation of both innate and adaptive immunity.

Keywords

Cytosolic DNA-sensing pathway, innate immunity, regulatory T cells, modified vaccinia virus Ankara, tumor immune-suppressive microenvironment, dendritic cells, myeloid cells, $CD8^+$ cytotoxic T cells, type I IFN, IFNAR, OX40, and immune checkpoint blockade (ICB).

Introduction

Immune checkpoint blockade (ICB) therapy utilizing antibodies targeting T cell inhibitory mechanisms has revolutionized how solid tumors are treated (Ribas and Wolchok, 2018; Wei et al., 2018; Zou et al., 2016). However, the majority of patients without pre-existing antitumor T cell responses do not respond to ICB therapy and one-third of the initial responders develop acquired resistance to this line of therapy likely due to cancer immuno-editing (Ribas and Wolchok, 2018; Schreiber et al., 2011; Zaretsky et al., 2016). Therefore, innovative approaches to rendering tumors sensitive to ICB therapy are urgently needed.

Viral-based cancer immunotherapy is a versatile and effective approach to alter tumor immunosuppressive microenvironment (TME) through multiple mechanisms, including the induction of innate immunity, immunogenic cell death in the infected immune and tumor cells, and activation of tumor-infiltrating dendritic cells (DCs), and antitumor CD8 and CD4 T cells, as well as depletion of immunosuppressive cells (Bommareddy et al., 2018; Davola and Mossman, 2019; Lemos de Matos et al., 2020; Russell et al., 2012; Workenhe and Mossman, 2014). As a result, intratumoral (IT) delivery of immunogenic viruses turns “cold” tumors into “hot” tumors, which renders them sensitive to other immunotherapeutic modalities including ICB (Chesney et al., 2018; Dai et al., 2017; Ribas et al., 2018; Wang et al., 2021; Zamarin et al., 2014).

Poxviruses are large cytoplasmic DNA viruses. Modified vaccinia virus Ankara (MVA) is a highly attenuated vaccinia virus that has been used extensively as a vaccine vector (Gilbert, 2013; Liu et al., 2021; Volz and Sutter, 2017). MVA infection of dendritic cells induces type I IFN via the cytosolic DNA-sensing pathway mediated by the DNA sensor cyclic GMP-AMP synthase (cGAS) and downstream signaling molecules such as STimulator of INterferon Genes (STING) (Dai et al., 2014). However, MVA encodes multiple inhibitors of the nucleic acid-sensing pathways. IT heat-inactivated MVA (Heat-iMVA) generates stronger antitumor immunity than IT live MVA, which requires $CD8^+$ T cells, Batf3-dependent $CD103^+/CD8\alpha$ cross-presenting dendritic cells (DCs), and STING-mediated cytosolic DNA-sensing pathway (Dai et al., 2017).

We designed our recombinant MVA virus to engage both innate and adaptive immunity in the tumor microenvironment. First, given the importance of the cGAS/STING pathway in innate immune-sensing of MVA and MVA-induced antitumor immunity (Dai et al., 2017; Deng et al., 2014; Woo et al., 2014), we deleted the E5R gene, encoding a cGAS inhibitor, from the MVA genome to generate MVAΔE5R, which induces much higher levels of type I IFN compared with MVA (Yang et al., 2021). Second, we engineered the virus to express two membrane-anchored transgenes, FMS-like tyrosine kinase 3 ligand **(**Flt3L) and OX40L. Flt3L is a growth factor for $CD103^+$ DCs and plasmacytoid DCs (Liu and Nussenzweig, 2010). OX40L is a co-stimulatory ligand for OX40, a member of the tumor necrosis factor (TNF) receptor superfamily expressed on activated CD4 and CD8 T cells as well as regulatory T cells (Croft, 2009). Here we used rMVA to designate MVAΔE5R-hFlt3L-mOX40L, which expresses human Flt3L and murine OX40L, and rhMVA to designate MVAΔE5R-hFlt3L-hOX40L, which expresses human Flt3L and human OX40L.

We observed that IT rMVA induces strong antitumor effects via the cGAS/STING-mediated DNA-sensing mechanism and the IFNAR/STAT1/STAT2 pathway. Depletion of $CD8^+$ T cells renders tumors resistant to rMVA therapy. IT rMVA dramatically reduces $OX40^{hi}$ regulatory T cells (Tregs) in the injected tumors via OX40L/OX40 interaction and IFNAR signaling. Taken together, our study strongly supports that rational engineering of MVA is an innovative strategy to deplete intratumoral $OX40^{hi}$ Tregs to enhance antitumor immunity.

Results

The rationale for engineering a recombinant MVA virus (rMVA) with deletion of E5R and expression of human FMS-like tyrosine kinase 3 ligand (hFlt3L) and murine OX40L (mOX40L) for cancer immunotherapy. Our previous work demonstrated that Batf3-dependent $CD103^+$ DCs are required for antitumor immunity induced by intratumoral (IT) delivery of heat-inactivated modified vaccinia virus Ankara (Dai et al., 2017). Flt3L is a growth factor that is important for DC development, especially for $CD103^+$ DCs and plasmacytoid DCs (Liu and Nussenzweig, 2010). To investigate whether human Flt3L (hFlt3L) expression on tumor cells affects tumor growth and tumor-infiltrating myeloid cell populations, we constructed a murine melanoma B16-F10 stable cell line that expresses membrane-bound hFlt3L, and subsequently implanted either B16-F10-hFlt3L or the parental B16-F10 cells into WT C57BL/6J mice (**Figure S1A**). We observed that expressing hFlt3L on tumor cells delayed B16-F10 tumor growth and prolonged the survival of tumor-bearing mice (**Figure S1B and S1C**). The percentages of $CD103^+$ DCs out of $CD45^+$ cells, as well as the absolute numbers of $CD103^+$ DCs per gram of B16-F10-hFlt3L, were increased in B16-F10-hFlt3L tumors compared with B16-F10 control tumors, whereas $CD11b^+$ DCs were at similar levels in both tumors (**Figure S1D**). These results indicate that hFlt3L expression on tumor cell surfaces facilitates the development and proliferation of $CD103^+$ DCs in the tumor microenvironment.

OX40L is a costimulatory molecule that interacts with its receptor OX40 expressed on T cells (Croft et al., 2009). OX40L on activated dendritic cells plays an important role in the generation of antigen-specific T cell responses (Murata et al., 2000). We constructed a B16-F10-mOX40L cell line that constitutively expresses murine OX40L on its surface (**Figure S1A**). B16-F10-mOX40L tumors grew slower than the parental B16-F10 tumors after implantation (**Figure S1B and S1C**), with higher percentages of Granzyme B^+ $CD8^+$ T cells compared with the parental B16-F10 cells (**Figure S1E**). The median survival of mice implanted with B16-F10-hFlt3L or B16-F10-mOX40L were 28 and 34 days, 8 or 14 days longer, respectively, than those implanted with the control B16-F10 (**Figure S1C).**

We recently discovered that the vaccinia E5R gene encodes a potent inhibitor of cGAS (Yang et al., 2021). MVAΔE5R infection of murine bone marrow-derived dendritic cells (BMDCs) induces

much higher levels of IFNB compared with MVA (**Figure S2A**). We compared the antitumor efficacy of MVA vs. MVAΔE5R in the B16-F10 melanoma unilateral implantation model in vivo (**Figure S2B**) and found that IT MVA prolonged the medium survival from 11 days in the PBS-treated group to 26 days, and IT MVAΔE5R resulted in 60% survival (**Figure S2C**). We also designed the following recombinant MVA viruses to evaluate the utility of hFlt3L and mOX40L individually expressed by MVAΔE5R (**Figure S2D**). MVAΔE5R-hFlt3L and MVAΔE5R-mOX40L expressed respective transgenes in infected BHK21 cells (**Figure S2E**). IT delivery of the two viruses resulted in higher numbers of IFN-γ^+ T cells in the spleens compared with MVA or MVAΔE5R, as determined by ELISPOT analysis (**Figure S2F and S2G**). These results suggest that expressing hFlt3L or mOX40L by recombinant MVA improves antitumor efficacy.

Based on these results, we designed an rMVA (MVAΔE5R-hFlt3L-mOX40L) by inserting two transgenes, a membrane-bound hFlt3L, and mOX40L into the E5R locus (**Figure 1A**). The hFlt3L and mOX40L are linked by a P2A self-cleaving sequence and their expression is driven by the vaccinia synthetic early/late promoter. We observed that both transgenes were expressed efficiently on the surface of infected B16-F10 murine melanoma cells and BMDCs at 24 h post-infection (**Figure 1B**). rMVA infection of BMDCs induced the expression of *Ifnb, Ifna4, Ccl4, Ccl5, Cxcl9, Cxcl10*, and *Il12p40* genes. Infection of BMDCs with rMVA induced cGAS-dependent *Ifnb* gene expression and IFN-β protein secretion at higher levels compared with MVA (**Figure 1C and 1D**). rMVA infection also induces DC maturation, as manifested by CD86 upregulation, determined by FACS, in a cGAS-dependent manner (**Figure 1E**).

Intratumoral injection (IT) of rMVA elicits strong antitumor immune responses that are dependent on cGAS-STING-mediated DNA sensing and STAT1/STAT2-mediated IFNAR-signaling pathway. To test whether cGAS/STING and STAT1/STAT2 are important for IT rMVA-induced antitumor immunity, cGAS$^{-/-}$, STING$^{Gt/Gt}$ (lacking function STING) (Sauer et al., 2011), STAT1$^{-/-}$, STAT2$^{-/-}$ or age-matched WT C57BL/6J mice were implanted with B16-F10 melanoma intradermally. When the tumors were established, they were injected with rMVA twice weekly. Whereas IT rMVA resulted in tumor eradication or delayed tumor growth in WT mice, neither STAT1$^{-/-}$ or STAT2$^{-/-}$ mice responded to this therapy, with median survival of 15 and 12 days, respectively, compared with 11 days in the mock-treated group (**Figure 1F and 1G**). IT

rMVA treatment of cGAS$^{-/-}$ or STING$^{Gt/Gt}$ mice extended median survival from 11 days in PBS control group to 18.5 days ($p = 0.0002$). However, all of the cGAS$^{-/-}$ or STING$^{Gt/Gt}$ mice died from tumor progression (**Figure 1F and 1G**). These results demonstrated that activation of the cGAS-mediated cytosolic DNA-sensing pathway, as well as the IFNAR/STAT1/STAT2 signaling, by IT rMVA, is critical for the generation of antitumor immunity.

IT rMVA results in myeloid cells influx into the injected tumors and induces IFN-β and other inflammatory cytokine production in a cGAS/STING-dependent manner. To elucidate mechanisms of action of rMVA, we first investigated myeloid cell dynamics and determined which cell types are infected after IT viral therapy. To do that, we used the murine B16-F10 tumor implantation model and injected the tumors with MVAΔE5R expressing mCherry. At one or two-days post-injection, we harvested the tumors and analyzed tumor-infiltrating immune cells. IT MVAΔE5R-mCherry injection led to an influx of neutrophils one day post-injection, which subsided after the second day, when monocytes started to increase in the tumor microenvironment (**Figure 2A**). Among the myeloid cell populations, macrophages were most heavily infected, as determined by mCherry expression in the infected cells, followed by monocytes, neutrophils, CD103^{+}, and CD11b^{+} DCs (**Figure 2B-2G**). T, B, or NK cells, however, were largely not infected by IT injected MVAΔE5R (**Figure 2G**).

To investigate the innate immune responses of tumors induced by IT rMVA and the role of the cytosolic DNA-sensing pathway in this process, we isolated tumors from WT or STING$^{Gt/Gt}$ mice one day post treatment with rMVA or PBS (mock control) and subjected them to bulk RNA-seq analyses. We observed striking upregulation of genes involved in immune activation, apoptosis, and downregulation of genes involved in oxidative phosphorylation (**Figure 2H and 2I**). We separated the immune activation genes into several subcategories, including cytokines and chemokines, interferon-stimulated genes (ISGs), activation markers, transcription factors, and other sensors. We found that rMVA treatment upregulated the expression of *Ifnb1*, *Ifng*, *Il-15*, *Il15ra*, *Ccl2*, *Ccl4*, *Ccl5*, *Cxcl9*, and *Cxcl10* in a STING-dependent manner (**Figure 2H and 2I**). We also observed up-regulation of DC activation markers, including *CD86* and *CD40*, and T cell activation markers, including *Gzma*, *Gzmb*, *Pfr1*, and *CD69,* as dependent on STING (**Figure 2H and 2I**). *Caspase 1*, *Caspase 3*, *Caspase 4*, *Caspase 8,* and *Fas* gene expression was also induced by IT

rMVA in WT mice but not in STING-deficient mice (**Figure 2H and 2I**). The expression of genes involved in oxidative phosphorylation was downregulated after IT rMVA injection in WT mice but not in STING-deficient mice (**Figure 2H and 2I**). Taken together, our results show that IT rMVA leads to infection and recruitment of myeloid cell populations and activation of innate immune responses in those cells via the cGAS/STING pathway.

IT rMVA generates stronger systemic and local anti-tumor immune responses compared with MVAΔE5R in a B16-F10 murine melanoma implantation model. To determine the immunological mechanism of rMVA-induced antitumor immune responses, we used a murine B16-F10 bilateral tumor implantation model. B16-F10 cells were intradermally implanted into both flanks of C57BL/6J mice. After tumors were established, we injected MVAΔE5R, rMVA, or PBS as a control, to the right-side tumors twice, three days apart. Spleens and both tumors were harvested 2 days after the second injection (**Figure 3A**). IT rMVA generated the highest numbers of tumor-specific IFN-γ^+ T cells in the spleens compared with those treated with MVAΔE5R or with PBS as determined by ELISpot assay (**Figure 3B and 3C**). In the injected tumors, IT rMVA resulted in stronger T cell activation with higher percentages and absolute numbers of granzyme B^+ $CD8^+$ and $CD4^+$ cells compared with MVAΔE5R, or PBS control groups (**Figure 3D-3F**). In the non-injected tumors, IT rMVA also induced more granzyme B^+ $CD8^+$ and $CD4^+$ T cells (**Figure 3G-3I**), demonstarting that IT rMVA enhances T cell activation both locally and systemically. IT rMVA also induced IFN-γ^+ TNF-α^+ $CD8^+$ and $CD4^+$ T cells in the injected tumors, indicating enhanced T cell effector function (**Figure 3J-3M**). Taken together, these results demonstrate that IT rMVA results in the activation of both $CD8^+$ and $CD4^+$ T cells in the injected and non-injected tumors, as well as in the generation of systemic antitumor immunity.

rMVA-induced antitumor immune responses are dependent on the cGAS/STING-mediated cytosolic DNA-sensing and STAT2-mediated type I IFN signaling pathways. We observed that the B16-F10-bearing cGAS, STING, or STAT2-deficient mice responded poorly to rMVA treatment (**Figure 1K and 1L**), which led us to hypothesize that the cGAS/STING-mediated cytosolic DNA-sensing and STAT2-dependent IFN signaling pathways are important for the generation of antitumor $CD8^+$ T cell responses. To test that hypothesis, cGAS, STING, or STAT2-deficient and age-matched C57BL/6J control mice were intradermally implanted with B16-F10 cells

into their right flanks. IT rMVA generated polyfunctional IFN-γ^+TNF-α^+CD8$^+$ and granzyme B$^+$ CD8$^+$ T cells in the injected tumors only in WT mice, whereas only IFN-γ^+CD8$^+$T cells were induced by IT rMVA in cGAS$^{-/-}$ and STING$^{Gt/Gt}$ mice (**Figure 3N-3Q**). IT rMVA failed to induce either IFN-γ^+, Granzyme B$^+$ CD8$^+$ cells, or IFN-γ^+TNF-α^+ T cells in STAT2$^{-/-}$ mice (**Figure 3N-3Q**). These results indicate that both the cGAS/STING and STAT2-mediated signaling pathways are crucial for rMVA-induced T cell activation.

IT rMVA depletes OX40^{hi} Tregs in the injected tumors. In addition to enhanced CD8$^+$ and CD4$^+$ T cell activation, we also observed that IT rMVA treatment resulted in a significant reduction of Tregs in the injected tumors (**Figure 4A and 4B**). The mean percentages of Tregs (Foxp3$^+$CD4$^+$) out of CD4$^+$ T cells were 23%, 45%, and 51% in rMVA, MVAΔE5R, or PBS-treated tumors, respectively (**Figure 4A and 4B**). The absolute numbers of Tregs in rMVA injected tumors were significantly reduced compared with the PBS-treated group (**Figure 4A and 4B**). In the non-injected tumors, however, we did not observe a reduction of the percentages of Tregs out of CD4$^+$ T cells after rMVA treatment (**Figure 4C**). The percentages of cleaved caspase-3$^+$ cells out of tumor-infiltrating Tregs from rMVA-treated tumors were much higher compared with those from PBS-treated tumors (**Figure 4D and 4E**). These results support that rMVA treatment triggers apoptosis in tumor-infiltrating Tregs.

To determine whether Tregs play a negative role in recombinant MVA-based virotherapy, we implanted B16-F10 cells intradermally into Foxp3-DTR mice. After the tumors were established, we treated the tumors with IT MVAΔE5R, which does not significantly reduce Tregs (**Figure 4F**). Although intraperitoneal administration of diphtheria toxin (DT) alone did not affect tumor growth or survival (**Figure 4G and 4H**), DT plus IT MVAΔE5R injection significantly improved therapeutic efficacy compared with IT MVAΔE5R alone (**Figure 4G and 4H**). These results suggest that Tregs play an inhibitory role in viral-based immunotherapy and intratumoral depletion of Tregs by rMVA is an important mechanism for potentiating antitumor immunity.

IT rMVA preferentially depletes OX40^{hi} Tregs via OX40L-OX40 interaction and IFNAR signaling. We hypothesized that OX40L expressed by rMVA-infected myeloid and tumor cells might be important in mediating the reduction of OX40^{hi} Tregs. We first compared the surface

expression of OX40 in various T cell populations within the tumor microenvironment. The mean percentages of $OX40^{hi}$ Tregs among $CD4^+$ Tregs were 51% compared with 5.6% of $OX40^{hi}$ conventional T (Tcov) cells and 1% of $OX40^{hi}$ $CD8^+$ T cells (**Figure 5A).** The mean fluorescence intensity (MFI) of OX40 was much higher in $CD4^+$ Tregs than those in Tcov and $CD8^+$ T cells **(Figure 5B and 5C)**. The high expression of OX40 was unique to tumor-infiltrating Tregs, because OX40 expression levels in Tregs from spleens or lymph nodes (LNs) were much lower than those from tumors (**Figure S3A**). Next, we compared the tumor-infiltrating $OX40^{hi}$ Treg population with or without IT rMVA treatment. IT rMVA treatment preferentially reduced the percentages of $OX40^{hi}$ Tregs out of total Tregs, as well as the absolute numbers of $OX40^{hi}$ Tregs per gram of tumors in the injected tumors (**Figure 5D and 5E**). In OX40-deficient mice, however, IT rMVA did not result in Treg reduction in the injected tumors (**Figure 5F**). Finally, we evaluated OX40L expression in both tumor cells and myeloid cells 2 days after IT rMVA. OX40L was detected on B16-F10, tumor-infiltrating macrophages, $CD103^+$ DCs, $CD11b^+$ DCs, neutrophils, and monocytes (**Figure S3B and S3C**). These results indicate that IT rMVA results in the OX40L expression in a variety of cell types including tumor and tumor-infiltrating myeloid cells and reduces tumor-infiltrating $OX40^{hi}$ Tregs likely via OX40-OX40L interaction.

To evaluate whether the IFNAR signaling pathway is involved in rMVA-mediated Treg reduction, we co-administered anti-IFNAR-1 antibody with rMVA into implanted B16-F10 melanoma twice three days apart. Tumors were harvested two days post-second injection (**Figure 5G**). Whereas IT rMVA reduced the percentages of $OX40^{hi}$ Treg out of Tregs as well as the percentages of Tregs out of $CD4^+$ T cells, co-administration of anti-IFNAR-1 antibody with rMVA reversed the reduction (**Figure 5H**). In addition, co-administration of anti-IFNAR-1 with rMVA resulted in lower percentages of Granzyme B^+ $CD8^+$ and $CD4^+$ T cells compared with IT rMVA alone (**Figure 5H**), which is consistent with the role of type I IFN in promoting $CD8^+$ and $CD4^+$ T cell activation. Taken together, our results provide strong evidence that IT rMVA results in the depletion of $OX40^{hi}$ Tregs in the injected tumors via OX40L-OX40 interaction, and this process is facilitated by type I IFN induced by rMVA infection in the injected tumors.

Tumor-infiltrating $OX40^{hi}$ Tregs and $OX40^{lo}$ Tregs have distinctive transcriptomic features. We observed that in the murine B16-F10 melanoma model, the percentage of $OX40^{hi}$ Tregs

252 in total Tregs positively correlated with tumor mass, suggesting that OX40^{hi} Tregs may represent
253 an immunosuppressive cell population during tumor progression (**Figure 6A**). To determine the
254 functional differences between OX40^{hi}, OX40^{lo}, and OX40$^{-/-}$Tregs, we intradermally implanted
255 B16-F10 cells into Foxp3^{gfp} and OX40$^{-/-}$Foxp3^{gfp} mice in a C57BL/6J background and FACS-
256 sorted OX40^{hi} and OX40^{lo} intratumoral Tregs from Foxp3^{gfp} mice and OX40$^{-/-}$ Tregs from OX40^{-}
257 $^{/-}$ Foxp3^{gfp} mice and compared their suppression function *in vitro*. Flow cytometry analysis showed
258 that OX40^{hi} Tregs isolated from tumors suppressed Tconv proliferation more strongly compared
259 with tumor-infiltrating OX40^{lo} Tregs or OX40$^{-/-}$ Tregs *in vitro* (**Figure 6B and 6C**). We also iso-
260 lated splenic Tregs from tumor-bearing Foxp3^{gfp} mice and found that the suppressive activities of
261 these cells were similar to those of OX40^{lo} Tregs or OX40$^{-/-}$ Tregs isolated from tumors (**Figure**
262 **6B and 6C**).
263
264 To explore the transcriptomic differences between OX40^{hi} and OX40^{low} Tregs isolated from tu-
265 mors and spleens, RNA-seq analysis was performed on sorted Treg populations from Foxp3-GFP
266 mice as described above. Multidimensional scaling (MDS) plot showed that OX40^{hi} and OX40^{lo}
267 Tregs from either spleens or tumors were segregated into distinct populations (**Figure 6D**).
268 Whereas splenic OX40^{hi} and OX40^{lo} Tregs were similar to each other at the transcriptomic level,
269 intratumoral OX40^{hi} and OX40^{lo} Tregs diverged from each other with 3309 upregulated genes and
270 3846 down-regulated genes (**Figure 6E**). Pathway analysis showed that the main transcriptomic
271 differences between splenic OX40^{hi} and OX40^{lo} Tregs were related to E2F targets and G2M check-
272 points, suggesting that OX40^{hi} Tregs are more proliferative compared with OX40^{lo} Tregs in the
273 spleens (**Figure 6F and 6G**). The upregulated genes in OX40^{hi} Tregs compared with OX40^{lo} Tregs
274 from tumors belonged to the following pathways, including cell proliferation, DNA repair, oxida-
275 tive phosphorylation, glycolysis, and the unfolded protein response (**Figure 6F and 6G**). Com-
276 pared with OX40^{lo} Tregs in the tumors, OX40^{hi} Tregs had lower expression of genes that belong
277 to type I and II IFN response and inflammation (**Figure 6F and 6G**). OX40^{hi} Tregs had higher
278 expression of *Casp3* and *Casp7*, suggesting that they might be more prone to apoptosis (**Figure**
279 **6H)**. In addition, OX40^{hi} Tregs had higher *Il2ra* expression compared with OX40^{lo} Tregs, which
280 may explain their stronger suppressive capacity through competition for IL2 in the tumor micro-
281 environment (**Figure 6H**). OX40^{hi} Tregs also had high expression of *Ccl3* and *Ccl4* chemokines
282 (**Figure 6H**), which have been implicated in chemoattraction of CCR5^{+} CD4^{+} and CD8^{+} T cells

and immune suppression (Patterson et al., 2016). FACS analyses confirmed higher *CD39* and *Ccr8* expression in OX40^{hi} tumor-infiltrating Tregs compared with OX40^{lo} tumor-infiltrating Tregs (**Figure 6I**).

Comparison of OX40^{hi} Tregs in tumors vs. spleens revealed striking differences in these two populations. OX40^{hi} Tregs in tumors have higher expression of chemokine receptors including *Ccr2, Ccr5, Ccr8, Cxcr3, and Cxcr6* as well as chemokines including *Ccl1, Ccl2, Ccl3, Ccl4, Ccl5, Ccl7, Ccl8, Ccl12, Ccl17, Ccl22, Cxcl2, and Cxcl9*, which suggest that they are migratory in response to chemokine cues in the developing tumors (**Figure S4A**). OX40^{hi} Tregs in tumors also express higher levels of *Il10, Ctla4, Tnfrsf18 (GITR)*, thus correlating with a more potent immunosuppressive function (**Figure S4B**). Furthermore, OX40^{hi} Tregs in tumors express higher levels of genes involved in glycolysis and oxidative phosphorylation (**Figure S4C and S4D**).

CD8$^+$ T cells are required for the antitumor effects induced by IT rMVA. To determine which cell populations are essential for tumor eradication by IT rMVA, we performed an antibody depletion experiment using anti-CD8 and/or anti-CD4 antibodies during rMVA treatment. The depleting antibodies were first given intraperitoneally two days before IT rMVA and then were given at the same time when mice were treated with IT rMVA (**Figure 7A**). Depletion of CD8$^+$ cells abrogated the therapeutic effect of rMVA (**Figure 7B and 7C**). Although CD4$^+$ T cell depletion resulted in a better response to rMVA treatment initially, however, the antitumor response did not persist in the CD4$^+$ T cell-depleted mice after IT rMVA treatment ended on day 42. 60% of mice died due to the recurrence of tumors. Mice with both CD4$^+$ and CD8$^+$ T cell-depleted behaved similarly to those with just CD8$^+$ T cell depletion (**Figure 7B and 7C**). These results suggested that CD8$^+$ T cells are required for tumor eradication in IT rMVA therapy, while CD4$^+$ T cells may be important for facilitating the generation of anti-tumor memory responses.

IT rMVA activates pre-existing CD8$^+$ T cells in the tumors, which is sufficient for the eradication of injected tumors. To determine whether local T cell activation or T cell recruitment from tumor-draining lymph nodes (TDLNs) is important for rMVA-induced antitumor effects in the injected tumors, we administered FTY720 (fingolimod), a modulator of the sphingosine-1-phosphate receptor, which blocks T cell egress from lymphoid organs. FTY720 was given

intraperitoneally one day before IT rMVA and was later given to the mice twice a week on the days when they were treated with IT rMVA (**Figure 7D**). FACS analysis confirmed that FTY720 treatment depletes $CD8^+$ and $CD4^+$ T cells in the blood (**Figure 7E and 7F**). We observed that FTY720 treatment alone did not affect tumor growth. Co-administration of FTY720 with IT rMVA treatment did not diminish the antitumor effect of IT rMVA (**Figure 7G and 7H**). When the surviving mice previously treated with IT rMVA alone or with IT rMVA plus FTY720 were challenged with a lethal dose of B16-F10 on the contralateral side at 7 weeks post tumor eradication, 80% of the mice in the rMVA plus FTY720 group and 100% of the mice in the rMVA alone group were able to reject tumor challenge (**Figure 7I**). No FTY720 was administered during the challenge phase. We analyzed T cells from both the injected tumors and TDLNs with or without FTY720 treatment, and found that Granzyme B^+CD8^+ T cells were increased after rMVA treatment with or without FTY720, indicating that IT rMVA directly activates preexisting antitumor $CD8^+$ T cells in the tumors without lymph node involvement (**Figure 7J and 7K**). In the FTY720-treated group, the percentages of Granzyme B^+CD8^+ T cells in the TDLNs were higher than that of the DMSO control group with rMVA injection (**Figure 7L**), indicating that the newly primed $CD8^+$ T cells were trapped in the TDLNs. These results indicate that IT rMVA-induced local activation of anti-tumor T cells is sufficient for the eradication of injected tumors.

Combination of IT delivery of rMVA with systemic administration of anti-PD-L1 antibody provides systemic antitumor therapeutic effects. B16-F10 tumors respond poorly to immune checkpoint blockade (ICB) therapy. To test whether the combination of systemic delivery of ICB antibody and IT rMVA therapy can overcome the resistance to ICB therapy, we used a bilateral B16-F10 implantation model and compared the antitumor efficacy of with IT rMVA alone vs. IT rMVA plus intraperitoneal (IP) delivery of anti-PD-L1 antibody (**Figure 8A**). IT rMVA alone eradicated 9 out of 10 injected tumors and delayed the growth of non-injected tumors. However, 90% of mice died eventually due to the growth of non-injected tumors (**Figure 8B and 8C**). By contrast, the combination of IP anti-PD-L1 antibody and IT rMVA significantly improved the antitumor therapeutic efficacy (**Figure 8B and 8C**). 80% of mice in the combination group rejected non-injected tumors and survived. These results demonstrated that the combination of systemic delivery of anti-PD-L1 antibody and IT rMVA generates synergistic systemic antitumor therapeutic effects, leading to the eradication of both injected and non-injected tumors.

IT rMVA is effective in generating antitumor T cell responses and controlling tumor growth in murine A20 B cell lymphoma and triple-negative breast cancer models. In addition to murine B16-F10 melanoma, we evaluated the therapeutic efficacy of IT rMVA in other murine tumor models. IT rMVA efficiently eradicated A20 B cell lymphoma tumors and resulted in 100% survival (**Figure 8D and 8E**). MMTV-PyMT is a transgenic mouse strain that develops multiple tumors in the mammary fat pads spontaneously, commonly used as a triple-negative breast tumor model. In the MMTV-PyMT mice, IT injection of rMVA resulted in delayed tumor growth compared with the PBS control group (**Figure 8F**). Similar to what we observed in the B16-F10 murine melanoma model, IT rMVA activated $CD8^+$ T cells in the tumors and reduced Tregs (**Figure 8G-8I**).

Clinical candidate rhMVA (MVAΔE5R-hFlt3L-hOX40L) induces innate immunity and promotes maturation of human monocyte-derived DCs (moDCs). For clinical applications, we generated an rhMVA expressing human Flt3L and human OX40L and with the deletion of E5R gene (**Figure S5A**). hFlt3l and hOX40L are membrane-bound ligands that were expressed on the surface of murine B16-F10 cells and human melanoma cell line, SK-MEL-28, after infection with rhMVA *in vitro* (**Figure S5B**). rhMVA induced higher levels of *ifnb* gene expression as well as *ccl4, ccl5, cxcl10, il1b, il6*, and *tnf* in moDCs compared with MVA (**Figure S5C**). rhMVA infection of moDCs induced the expression of CD86 on the cell surface, which is indicative of DC maturation (**Figure S5D**).

To test whether *ex vivo* infection of human tumor samples with rhMVA could induce phenotypic changes of tumor-infiltrating lymphocytes (TILs), we obtained skin biopsy samples from patients with extramammary paget's disease (EMPD), infected the processed tissues with rhMVA, and analyzed TILs 24 h later (**Figure 8K**). We found that rhMVA-infected samples exhibited upregulation of granzyme B on $CD8^+$ T cells as well as reduction of Tregs compared with the paired control samples (**Figure 8L**). These results are consistent with what we observed in various murine tumors treated with rMVA *in vivo*, further supporting rhMVA as a potential clinical candidate for the treatment of various human cancers.

Discussion

Preclinical and clinical studies have shown that viral-based immunotherapeutics can alter immunosuppressive tumor microenvironment to enhance antitumor effects and overcome resistance to immune checkpoint blockade antibody therapy. Our previous study using heat-inactivated modified vaccinia virus Ankara (heat-iMVA) demonstrated that induction of innate immunity via the STING-dependent pathway in the tumor microenvironment is important for the generation of systemic antitumor immunity (Dai et al., 2017), which is also dependent on $CD8^+$ T cells and Batf3-dependent $CD103^+/CD8\alpha^+$ DCs. Based on this concept, we engineered a recombinant MVA (rMVA) with deletion of the vaccinia E5R gene, which encodes an inhibitor of cGAS, and with the expression of two membrane-bound transgenes, human Flt3L, and murine OX40L. Here we show that rMVA activates innate immunity via the cGAS/STING pathway and the IFNAR positive feedback loop, and also reduces $OX40^{hi}$ regulatory T cells via OX40L-OX40 interaction in the injected tumors.

Poxviruses are large cytoplasmic DNA viruses. DNAs from the parental viral genome and the replicated progeny viral genome are potent stimuli for activating the cytosolic DNA-sensing pathway mediated by cGAS/STING. The vaccinia E5R gene is highly conserved among the orthopoxvirus family which includes variola virus, the causative agent of smallpox, and vaccinia virus, the laboratory strain that leads to the eradication of smallpox. MVAΔE5R infection of BMDCs induces higher levels of type I IFN compared with MVA, which is dependent on cGAS. Similarly, rMVA infection of BMDCs induces much higher levels of IFN compared with MVA. rMVA infection also induces cGAS-dependent DC maturation. IT delivery of rMVA generates stronger local and systemic antitumor effects compared with MVA, or MVAΔE5R. Using cGAS, STING, STAT1, and STAT2-deficient mice, we demonstrated that the cGAS/STING-mediated cytosolic DNA-sensing and STAT1/STAT2-mediated type I IFN pathways are required for the generation of antitumor immunity by rMVA. In addition to the induction of innate immunity, IT delivery of rMVA reduces $OX40^{hi}$ $Foxp3^+CD4^+$ regulatory T cells in the injected tumors via OX40L/OX40 interaction which is reversed in the presence of anti-IFNAR antibody. Furthermore, using FTY720 to block lymphocyte egress from lymphoid organs, we demonstrated that IT rMVA-induced local activation of tumor-specific T cells in the injected tumors is sufficient for its eradication.

To understand why the cGAS/STING pathway is important in rMVA-induced antitumor immunity, we first evaluated what cell populations in the tumor microenvironment are preferentially infected by the virus. Using MVAΔE5R-expressing the mCherry reporter under the vaccinia virus synthetic early/late promoter, we found that the myeloid cell populations including macrophages, monocytes, neutrophils, and dendritic cells are targeted by the virus, whereas lymphocytes are largely spared. RNA-seq analyses of tumor tissues isolated 24 h post IT rMVA revealed marked upregulation in the expression of *Ifnb*, inflammatory cytokines and chemokines, DC activation markers, IFN-stimulated genes, and genes involved in apoptosis in WT mice, but not in STING-deficient mice. On the contrary, the expression of genes involved in oxidative phosphorylation was reduced in rMVA-treated tumors in WT mice, but not in STING-deficient mice.

We next addressed how innate immune activation, for example, the cGAS/STING pathway and type I IFN signaling in the tumor microenvironment, affects the activation status of tumor-infiltrating T cells. Using cGAS, STING, or STAT2-deficient mice or intratumoral delivery of anti-IFNAR antibody, we found that the activation of intratumoral $CD8^+$ and $CD4^+$ T cells depends on the generation of type I IFN and IFN signaling in the tumor microenvironment. This is consistent with a published report that type I IFN signaling drives antigen-independent expression of granzyme B on memory $CD8^+$ T cells in a respiratory viral infection model (Kohlmeier et al., 2010). While IT rMVA was ineffective in shrinking tumors when $CD8^+$ T cells were depleted, $CD4^+$ T cells depletion did not impede tumor control initially. However, tumors regrew when both the anti-CD4 antibody and rMVA treatment were discontinued. We interpret these results as the following: As anti-CD4 antibody removes both Tcov and Tregs from tumors and circulation, mice were able to control tumor growth with activated $CD8^+$ T cells which function better in the absence of Tregs. However, they fail to develop antitumor memory $CD8^+$ T cells in the absence of helper $CD4^+$ T cells.

Our study demonstrates that IT rMVA preferentially reduces $OX40^{hi}$ Tregs in injected tumors via the OX40L-OX40 interaction and this process is promoted by type I IFN in the tumor microenvironment. We found that OX40 is preferentially expressed by intratumoral Tregs and its expression correlates with tumor weight in murine melanoma models. $OX40^{hi}$ Tregs isolated from tumors are more immunosuppressive compared with $OX40^{low}$ Tregs. Comparison of the transcriptomes of

436 OX40^{hi} and OX40^{lo} intratumoral Tregs revealed that OX40^{hi} Tregs are more proliferative, meta-
437 bolically active, and immunosuppressive. Therefore, targeting intratumoral OX40^{hi} Tregs by
438 rMVA expressing OX40L is a logical approach to deplete this cell population within the tumors
439 but not in the periphery, and thereby improving the efficacy of immunotherapy without unwanted
440 autoimmunity. We found that OX40^{hi} Tregs expressed higher levels of CCR8 compared with
441 OX40^{lo} Tregs. CCR8^{+} Tregs have been reported to play important roles in immune suppression in
442 mice and humans (Barsheshet et al., 2017; Coghill et al., 2013; Plitas et al., 2016). Targeting
443 CCR8^{+} Tregs using an anti-CCR8 antibody showed therapeutic benefits for cancer treatment and
444 cancer vaccines in preclinical models (Villarreal et al., 2018). In addition to CCR8^{+}, OX40^{hi} Tregs
445 also expressed higher levels of *Il2ra, Ctla4, Tnfrsf18, Il10*, and *Cd39*, which are consistent with
446 their immunosuppressive functions (Chinen et al., 2016; Cohen et al., 2010; Leone et al., 2018;
447 Maj et al., 2017; Wing et al., 2008; Zappasodi et al., 2019).
448
449 Our results also showed that intratumoral OX40^{hi} Tregs had marked upregulation of genes in-
450 volved in oxidative phosphorylation compared with intratumoral OX40^{lo} Tregs or with OX40^{hi}
451 Tregs in the spleens. Several recent studies highlight the potential of modulating Treg stability and
452 functions through metabolic control (Field et al., 2020; He et al., 2017; Weinberg et al., 2019;
453 Zappasodi et al., 2021). How IT rMVA alters metabolism of OX40^{hi} Tregs via OX40L-OX40
454 interaction and the role of IFNAR signaling on Tregs on metabolic alterations and apoptosis will
455 be addressed in future studies.
456
457 FTY720 (fingolimod), a sphingosine 1-phosphate receptor (S1P-R) agonist, is a novel immuno-
458 modulatory agent that blocks lymphocyte egress from lymphoid organs, FDA-approved for the
459 treatment of relapsing multiple sclerosis. We observed that FTY720 did not affect the antitumor
460 effects of rMVA in the injected tumors, despite trapping CD8^{+} T cells in the TDLNs, supporting
461 our hypothesis that local activation of CD8^{+} T cells in the injected tumors is sufficient to eliminate
462 the injected tumors. We provided evidence that type I IFN induction by rMVA in the injected
463 tumors facilitates the proliferation and activation of CD8^{+} T cells. In addition, IFN contributes to
464 the depletion of OX40^{hi} Tregs via the OX40L-OX40 ligation on Tregs. Removal of immunosup-
465 pressive OX40^{hi} Tregs in the rMVA-infected tumors leads to the activation of CD8^{+} and CD4^{+} T
466 cells.

Taken together, we propose the following working model for elucidating the mechanisms of action of rMVA (**Figure S6**). After intratumoral injection with rMVA, both tumors and tumor-infiltrating myeloid cells are infected by the virus, which leads to the expression of hFlt3L and mOX40L transgenes on the cell surface, as well as the induction of type I IFN and proinflammatory cytokines and chemokines via the cGAS/STING-dependent cytosolic DNA-sensing pathway from the resident and recruited tumor-infiltrating myeloid cells. Type I IFN plays an important role in activating DCs and tumor-infiltrating $CD8^+$ and $CD4^+$ T cells. In addition, OX40L expression on infected tumor and myeloid cells leads to the depletion of $OX40^{hi}$ Tregs via OX40L-OX40 interaction, which further enhances the antitumor activities of $CD8^+$ and $CD4^+$ T cells. Therefore, rMVA engages both innate and adaptive immunity to generate local and systemic antitumor effects, which are amplified in the presence of immune checkpoint blockade antibodies.

OX40 modulating agents have been explored for enhancing antitumor effects through targeting Tregs. For example, the combination of anti-OX40 agonist antibody with cyclophosphamide triggers activation and apoptosis of intratumoral Tregs while causing Treg expansion in the TDLN and spleens (Hirschhorn-Cymerman et al., 2009). This combination also promotes tumor-killing activities of antigen-specific adoptively transferred $CD4^+$ T cells (Hirschhorn-Cymerman et al., 2012). In addition, intratumoral delivery of low doses of anti-CTLA-4 and anti-OX40 antibodies together with TLR9 agonist CpG leads to Treg depletion at the injected site but not in the non-injected site and generates systemic antitumor immunity (Marabelle et al., 2013). Our RNA-seq results confirmed that $OX40^{hi}$ intratumoral Tregs express higher levels of CTLA-4 as well as other immune suppressive markers compared with $OX40^{lo}$ Tregs. Therefore, our approach of using a recombinant immune-activating virus to express OX40L represents a novel strategy to deplete $OX40^{hi}$ immunosuppressive Tregs. Compared with anti-OX40 agonist antibody approach, our engineered virus expressing OX40L might be more specific in targeting $OX40^{hi}$ Tregs within the tumor microenvironment. IFN-inducing ability of the virus also promotes Treg depletion. The combination of intratumoral delivery of rMVA expressing mOX40L with systemic delivery of anti-PD-L1 antibody generates synergistic antitumor effects. This is in contrast to two reports showing that concurrent administration of anti-PD1 antibody leads to reduced efficacy of anti-

497 OX40 antibody due to apoptosis of activated T cells (Messenheimer et al., 2017; Shrimali et al.,
498 2017).

Figure 1

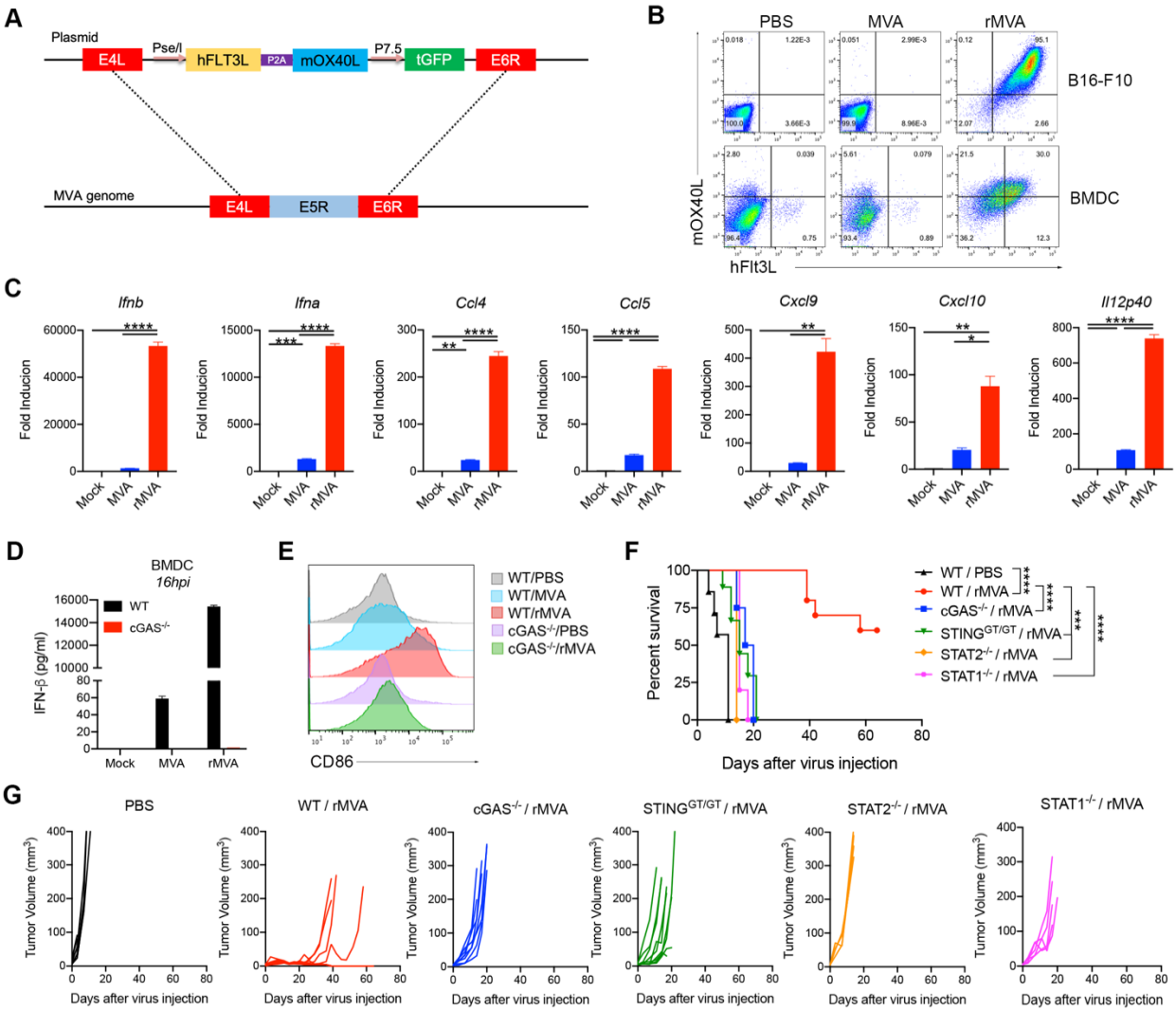

Figure 1. Intratumoral injection (IT) of rMVA elicits strong antitumor immune responses that is dependent on cGAS-STING and STAT1/STAT2.

(A) Schematic diagram for the generation of rMVA through homologous recombination.

(B) Representative flow cytometry plots of expression of hFlt3L or mOX40L by rMVA-infected B16-F10 cells and BMDCs.

(C) Relative mRNA expression levels of *Ifnb*, *Ifna*, *Ccl4*, *Ccl5*, *Cxcl9, Cxcl10* and *Il12p40* in BMDCs infected with MVA or rMVA. Data are means ± SD (*n=3; *P < 0.05, **P < 0.01, ***P < 0.001, ****P < 0.0001, t test).*

(D) Concentrations of secreted IFN-β in the medium of WT or $cGAS^{-/-}$ BMDCs infected with MVA or rMVA. Data are means ± SD.

(E) Mean fluorescence intensity of CD86 expressed by WT or $cGAS^{-/-}$ BMDCs infected with MVA or rMVA.

(F) Kaplan-Meier survival curve of mice treated with rMVA or PBS in a unilateral B16-F10 implantation model (*n=5~10; ***P < 0.001, ****P < 0.0001, Mantel-Cox test*).

(G) Tumor growth curve of mice treated with rMVA or PBS in a unilateral B16-F10 implantation model.

Figure 2

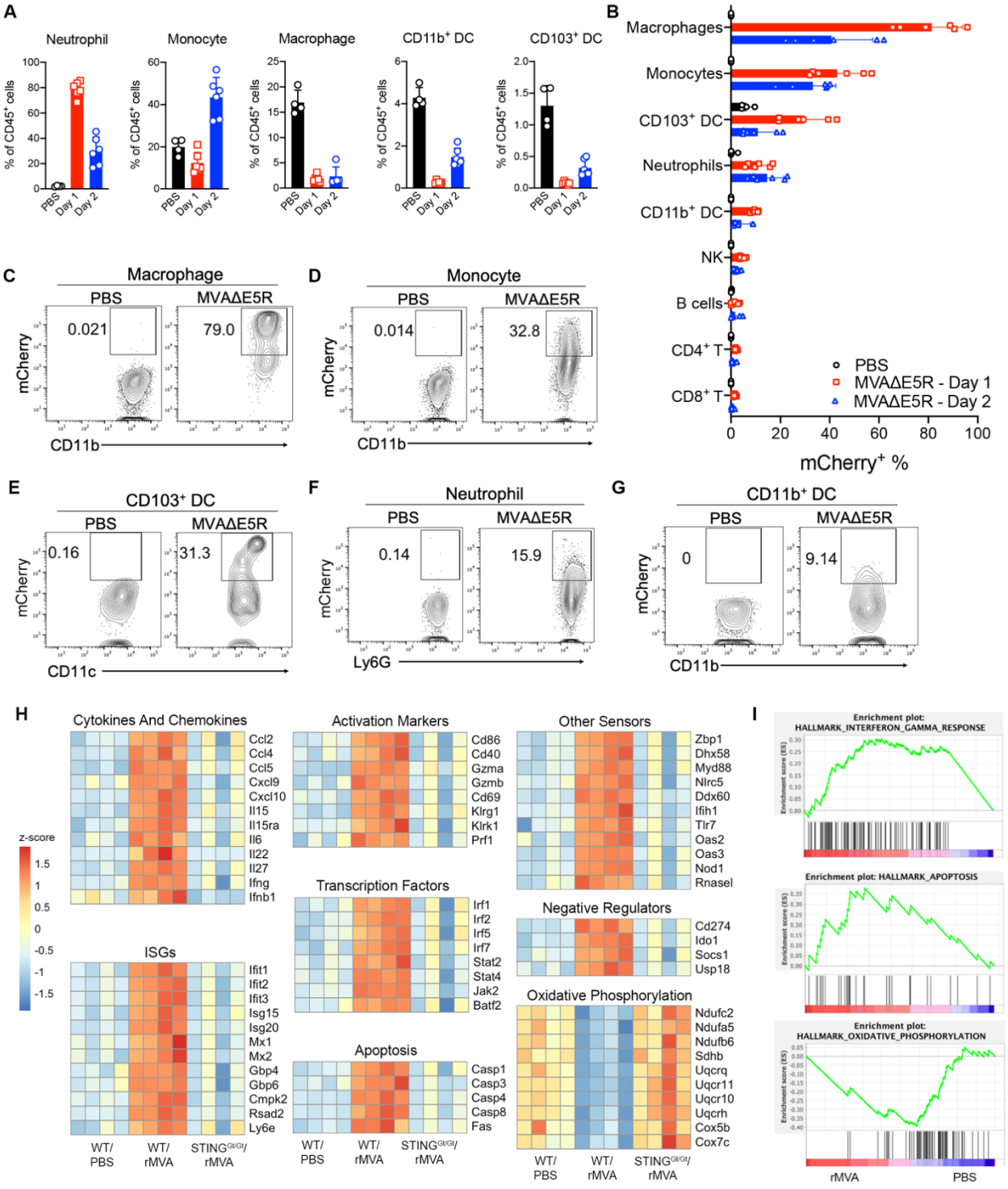

Figure 2. Influx of myeloid cells into MVAE5R-treated tumors and induction of IFN-β and other inflammatory cytokine production in a cGAS/STING-dependent manner.

(A) Percentages of neutrophils, monocytes, macrophages, $CD103^+$ DCs and $CD11b^+$ DCs in the MVAΔE5R-treated tumors. Mice were intradermally implanted with B16-F10 cells. 7 days post implantation, tumors were injected with MVAΔE5R-mCherry or PBS as control and harvested 1- or 2-days post injection for myeloid cell analysis. Data are means ± SD (*n=4~6)*.

(B) Percentages of $mCherry^+$ immune cells. Data are means ± SD (*n=4~6)*.

(C-G) Representative flow cytometry plots of $mCherry^+$ immune cells.

(H) Heatmap of gene expression from bulk tumor RNA-seq analysis.

(I) Gene set enrichment analysis.

Figure 3

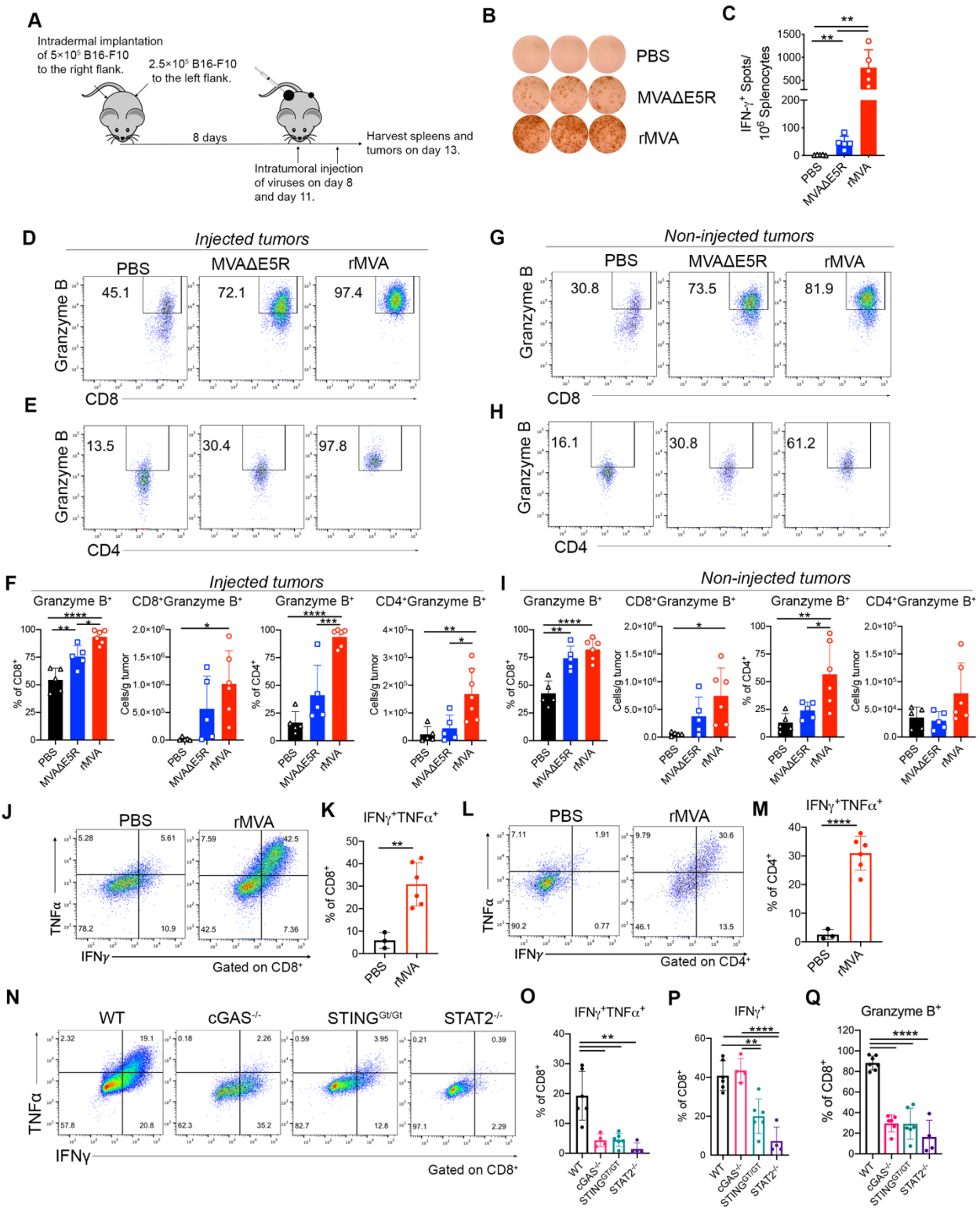

Figure 3. IT rMVA generates strong systemic and local anti-tumor immune responses which is dependent on cGAS/STING/STAT2 pathways.

(A) Schematic diagram of IT rMVA or MVAΔE5R for ELISpot assay and TIL analysis in a murine B16-F10 melanoma implantation model.

(B) Representative images of IFN-γ^+ spots from ELISpot assay.

(C) Statistical analysis of IFN-γ^+ splenocytes from MVAΔE5R, rMVA or PBS-treated mice. Data are means ± SD (*n=5 or 6; **P < 0.01, t test).*

(D-E) Representative flow cytometry plots of Granzyme B^+ $CD8^+$ (D) and Granzyme B^+ $CD4^+$ cells (E) in the injected tumors.

(F) Percentages and absolute number of Granzyme B^+ $CD8^+$ and Granzyme B^+ $CD4^+$ cells in the injected tumors. Data are means ± SD (*n=5 or 6; *P < 0.05, **P < 0.01, ***P<0.001, ****P < 0.0001, t test).*

(G-H) Representative flow cytometry plots of Granzyme B^+ $CD8^+$ (G) and Granzyme B^+ $CD4^+$ cells (H) in the non-injected tumors.

(I) Percentages and absolute number of Granzyme B^+ $CD8^+$ (J) and Granzyme B^+ $CD4^+$ (K) cells in the non-injected tumors. Data are means ± SD (*n=5 or 6; *P < 0.05, **P < 0.01, **** P < 0.0001, t test).*

(J-M) Representative flow cytometry plots and statistical analysis of IFNγ^+TNFα^+ $CD8^+$ (J, K) and IFNγ^+TNFα^+ $CD4^+$ cells (L, M) in the injected tumors. Data are means ± SD (*n=3 or 6; **P < 0.01, ****P < 0.0001, t test).*

(N) Representative flow cytometry plots of IFNγ^+TNFα^+ $CD8^+$ T cells in the injected tumors harvested from WT, $cGAS^{-/-}$, $STING^{Gt/Gt}$, and $STAT2^{-/-}$ mice.

(O) Percentages of IFNγ^+TNFα^+ $CD8^+$ T cells in the injected tumors from WT, $cGAS^{-/-}$, $STING^{Gt/Gt}$ and $STAT2^{-/-}$ mice. Data are means ± SD (*n=4~6; **P < 0.01, t test).*

(P) Percentages of IFNγ^+ $CD8^+$ T cells in the injected tumors from WT, $cGAS^{-/-}$, $STING^{Gt/Gt}$ and $STAT2^{-/-}$ mice. Data are means ± SD (*n=4~6; **P < 0.01, t test).*

(Q) Percentages of Granzyme B^+ $CD8^+$ T cells in the injected tumors from WT, $cGAS^{-/-}$, $STING^{Gt/Gt}$ and $STAT2^{-/-}$ mice. Data are means ± SD (*n=4~6; ****P < 0.0001, t test).*

Figure 4

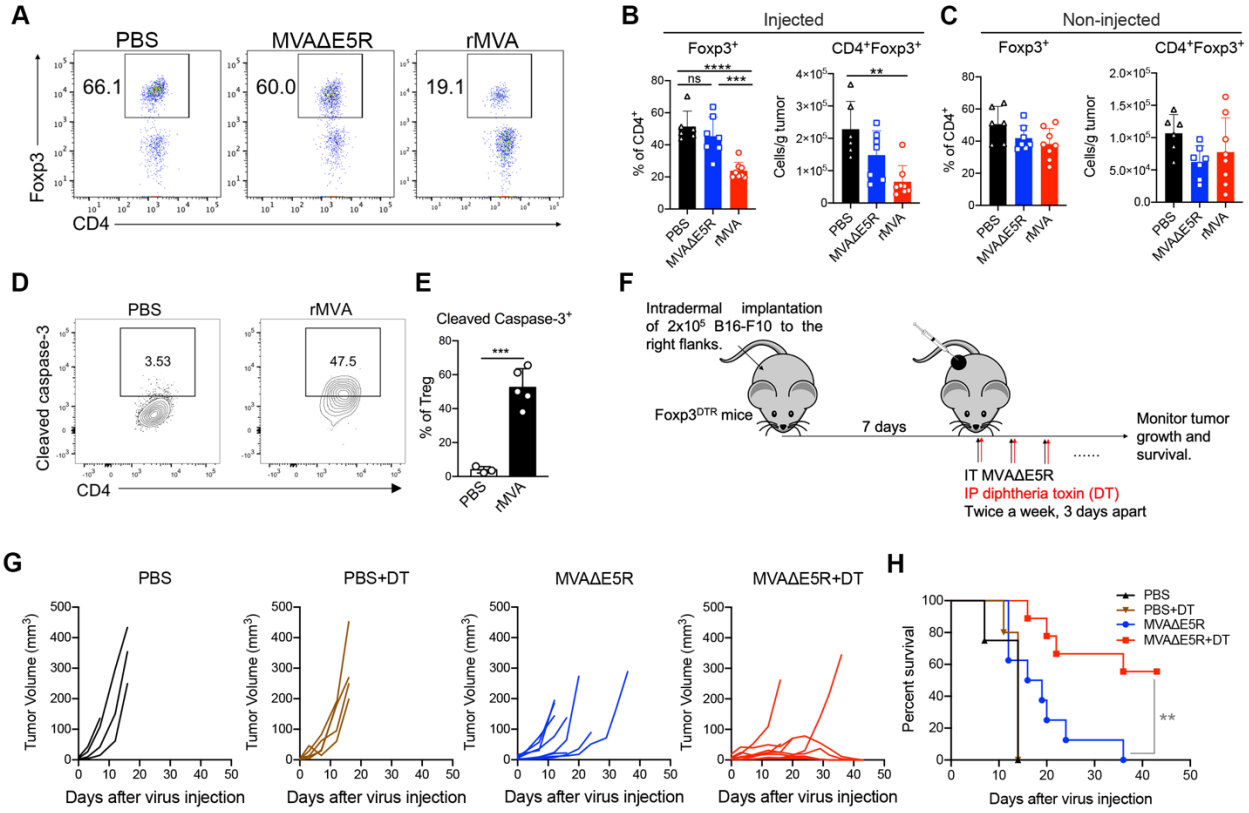

Figure 4. IT rMVA depletes OX40^{hi} Tregs in the injected tumors to promote anti-tumor therapy.

(A) Representative flow cytometry plots of Foxp3^{+}CD4^{+} cells in the injected tumors. Mice were treated as described in Fig. 3A.

(B-C) Percentages and absolute number of Foxp3^{+}CD4^{+} cells in the injected (B) and non-injected (C) tumors. Data are means ± SD (*n=6-8; **P < 0.01, ***P<0.001, ****P < 0.0001, t test).*

(D-F) Mice were intradermally implanted with B16-F10 cells. Tumors were injected with rMVA or PBS as control after 7 days post implantation and harvested 2-days post injection.

(D) Representative flow cytometry plots of cleaved caspase-3^{+} Tregs in the injected tumors.

(E) Percentages of cleaved caspase-3 in tumor infiltrating-Tregs by flow cytometry. Data are means ± SD (*n=3-5; **P < 0.01, t test).*

(F) Schematic diagram of IT rMVA in the presence or absence of DT in a unilateral B16-F10 melanoma implantation model in Foxp3^{DTR} mice.

(G) Tumor growth curves of mice treated with rMVA or PBS.

(H) Kaplan-Meier survival curves of mice treated with rMVA or PBS (*n=5-10; **P < 0.01, Mantel-Cox test*).

Figure 5

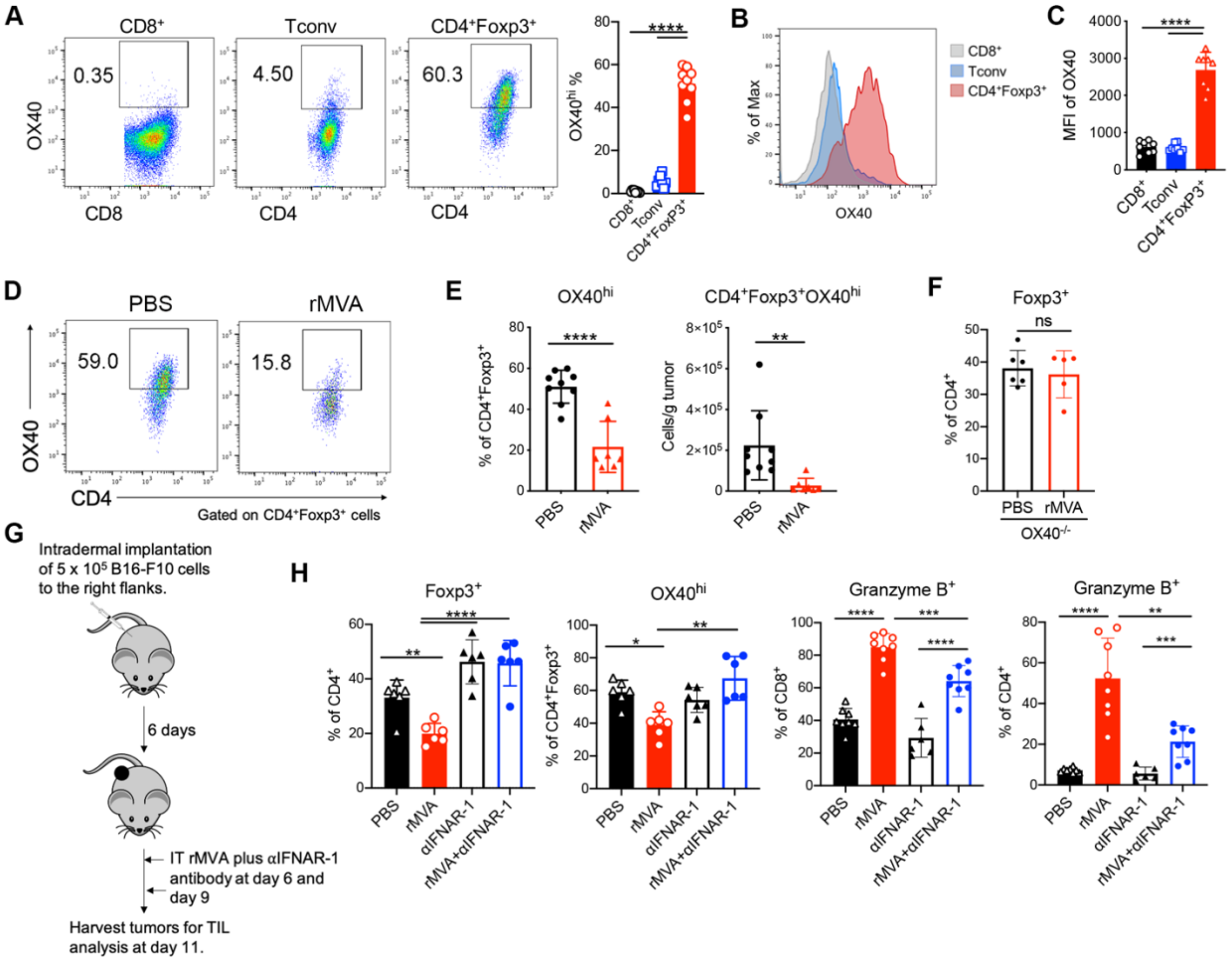

Figure 5. IT rMVA preferentially depletes OX40^{hi} Tregs in the injected tumors in a type I IFN signaling dependent manner.

(A) Representative flow cytometry plots of OX40 expression on tumor infiltrating CD8$^+$, Tconv, and CD4$^+$Foxp3$^+$ T cells in tumors 15 days after implantation. Mice were treated as described in Fig. 3A.

(B-C) Representative flow cytometry plots and statistical analysis of mean fluorescence intensity of OX40 on tumor-infiltrating CD8$^+$, Tconv, and CD4$^+$Foxp3$^+$ T cells. Data are means ± SD in (C) (*n=6~8; ****P < 0.0001, t test).*

(D) Representative flow cytometry plots of OX40^{hi}CD4$^+$Foxp3$^+$ in the injected tumors. Mice were treated as described in Fig. 3A.

(E) Percentages and absolute number of OX40^{hi}CD4$^+$Foxp3$^+$ T cells in the injected tumors. Data are means ± SD (*n=7 or 9; **P<0.01, ****P < 0.0001, t test).*

(F) Percentages of CD4$^+$Foxp3$^+$ T cells in the injected tumors from WT and OX40$^{-/-}$ mice. Mice were treated as described in Fig. 3A. Data are means ± SD (*n=5 or 6; t test).*

(G) Schematic diagram of IT rMVA in the presence or absence of IT αIFNAR-1 antibody in a unilateral B16-F10 melanoma implantation model.

(H) Percentages of CD4$^+$Foxp3$^+$ and OX40^{hi}CD4$^+$Foxp3$^+$ T cells in the injected tumors. Data are means ± SD (*n=6; *P<0.05, **P<0.01, ****P < 0.0001, t test).*

(I) Percentages of CD8$^+$Granzyme B$^+$ and CD4$^+$Granzyme B$^+$ T cells in the injected tumors. Data are means ± SD (*n=6; **P<0.01, ***P<0.001, ****P < 0.0001, t test).*

Figure 6

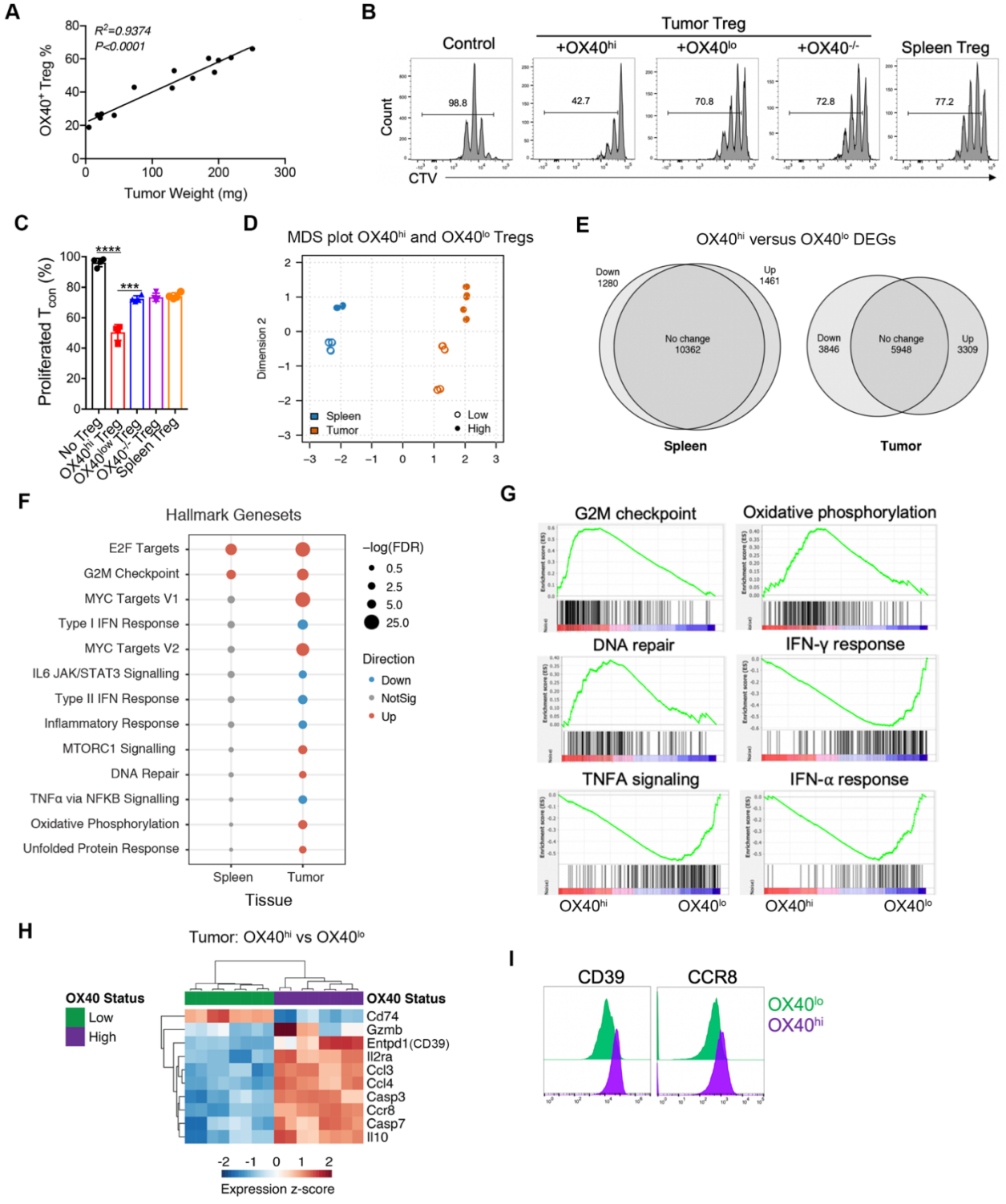

Figure 6. Tumor-infiltrating OX40^{hi} Tregs and OX40^{low} Tregs have distinctive transcriptomic features.

(A) Correlation of the percentages of OX40^{hi} Tregs in the tumors with tumor weight. Mice were implanted with B16-F10 tumors intradermally. Tumors with different sizes were analyzed for OX40 expression on tumor-infiltrating Tregs.

(B-C) Representative flow cytometry plots (B) and percentage of T_{con} proliferation (C) as measured by CTV dye dilution co-cultured with tumor OX40^{hi}, OX40^{low}, OX40$^{-/-}$ Tregs or spleen Tregs. Data are means ± SD in (C) (***P < 0.001; ****P < 0.0001, t test).*

(D) Multidimensional scaling (MDS) plot of RNA-seq results of OX40^{hi} and OX40^{low} Tregs from B16-F10 tumors.

(E) Venn diagram of the relationship of differential gene expression (DEGs) of OX40^{hi} Tregs vs. OX40^{lo} Tregs isolated from spleens and tumors.

(F) Gene set analysis of upregulated or downregulated genes comparing OX40^{hi} Tregs vs. OX40^{lo} Tregs isolated from spleens and tumors.

(G) Gene Set Enrichment Analysis (GSEA) of upregulated or downregulated genes comparing transcriptomes of OX40^{hi} Tregs vs. OX40^{lo} Tregs isolated from tumors.

(H) Heatmap of selected genes upregulated or downregulated genes in OX40^{hi} Tregs vs. OX40^{lo} Tregs isolated from tumors.

(I) Representative FACS plot showing the expressions of CD39 and CCR8 on OX40^{hi} Tregs and OX40^{lo} Tregs isolated from tumors.

Figure 7

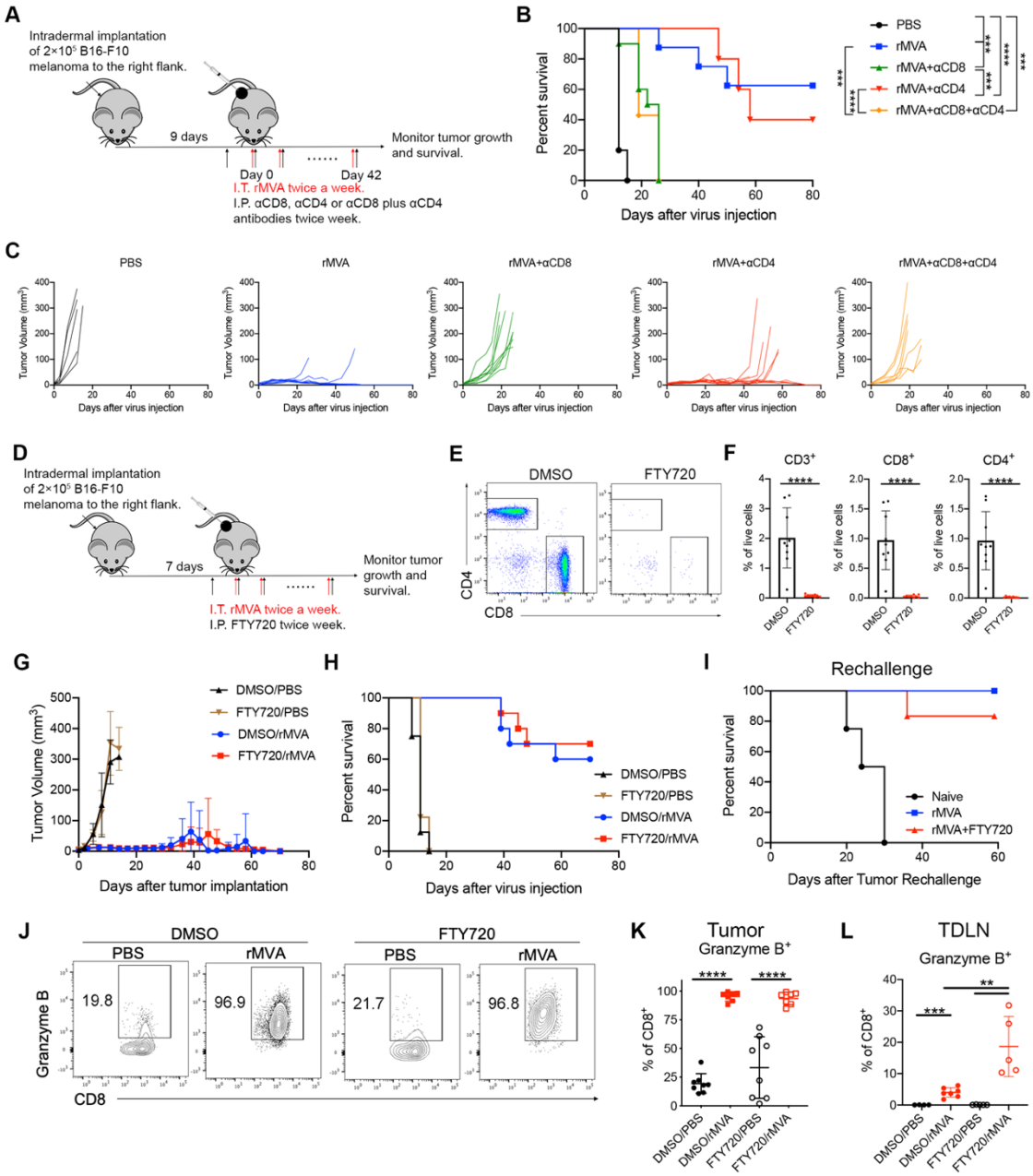

Figure 7. Local activation of $CD8^+$ T cells is sufficient for rMVA-mediated tumor eradication.

(A) Schematic diagram of IT rMVA in the presence or absence of depleting antibodies for CD8 and/or CD4 in a unilateral B16-F10 melanoma implantation model.
(B) Kaplan-Meier survival curves (*n=5~10; ***P < 0.001, ****P < 0.0001, Mantel-Cox test*).
(C) Tumor growth curves.
(D) Schematic diagram of IT rMVA in the presence or absence of FTY720 in a unilateral B16-F10 melanoma implantation model.
(E) Representative flow cytometry plot of $CD8^+$ and $CD4^+$ T cells in the PBL of mice treated with FTY720.
(F) Percentages of $CD8^+$ and $CD4^+$ T cells in the PBL of mice treated with FTY720. Data are means ± SD (*n=10; ****P < 0.0001, t test).*
(G) Tumor growth curves.
(H) Kaplan-Meier survival curves (*n=10*).
(I) Kaplan-Meier survival curves of survived mice from (H) or naïve mice challenged with $1x10^5$ B16-F10 cells at the contralateral side (*n=5 or 6*).
(J) Representative flow cytometry plots of Granzyme B^+CD8^+ T cells in the injected tumors.
(K) Percentages of Granzyme B^+CD8^+ T cells in the injected tumors. Data are means ± SD (*n=8; ****P < 0.0001, t test).*
(L) Percentages of Granzyme B^+CD8^+ T cells in the tumor-draining lymph nodes. Data are means ± SD (*n=6~8; **P < 0.01, ***P < 0.001, t test).*

Figure 8

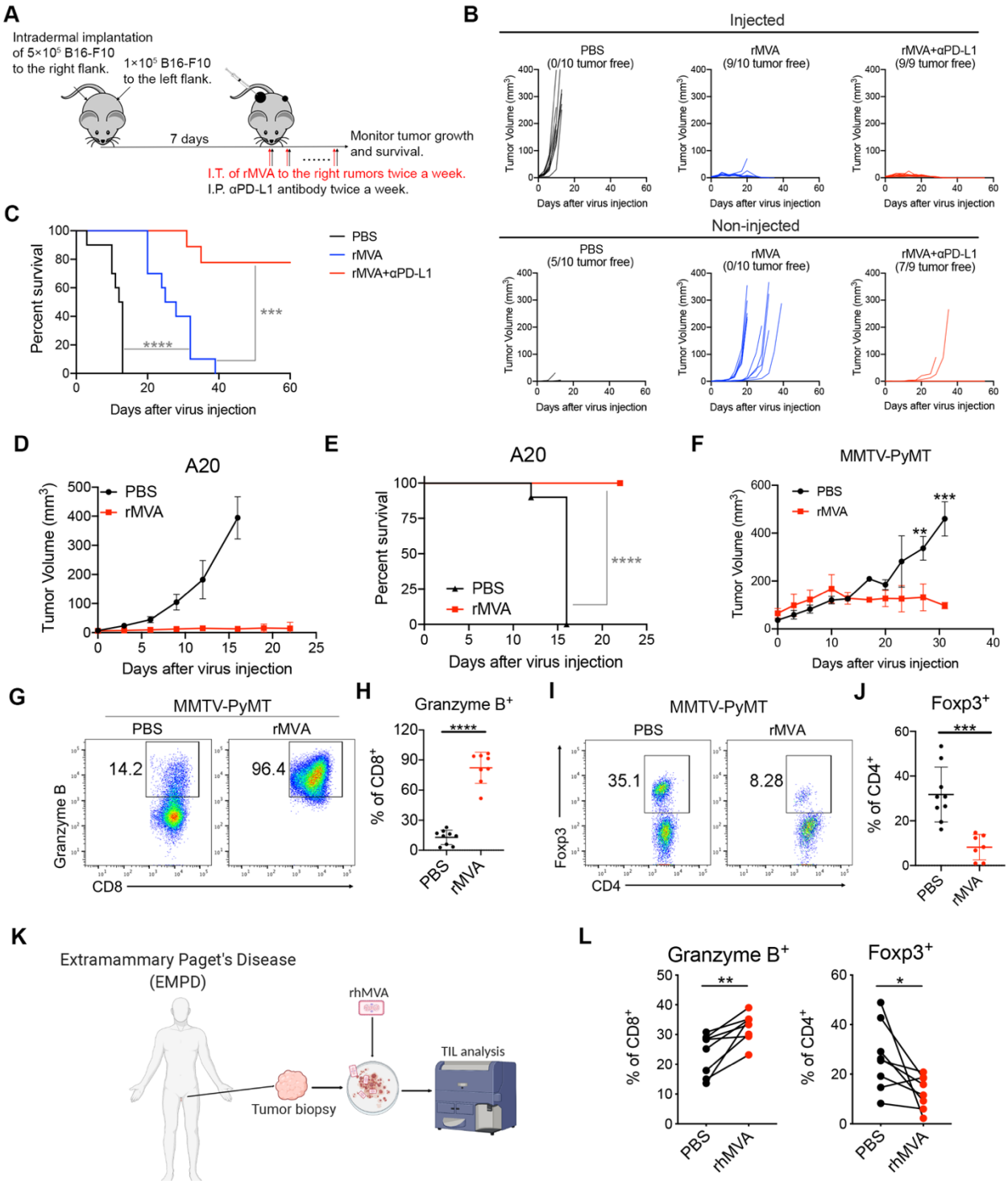

Figure 8. IT rMVA elicits strong antitumor immunity in multiple murine tumor models.
(A) Schematic diagram of IT rMVA in combination with IP αPD-L1 antibody in a bilateral B16-F10 melanoma implantation model.
(B) Tumor growth curves.
(C) Kaplan-Meier survival curves (*n=9 or 10; **** P < 0.0001, Mantel-Cox test*).
(D) Tumor growth curves of mice treated with IT rMVA in an A20 B cell lymphoma implantation model.
(E) Kaplan-Meier survival curves (*n=10; ****P < 0.0001, Mantel-Cox test*).
(F) Tumor growth curves in the PyMT-MMTV breast tumor model. Data are means ± SD (*n=5; **P < 0.01, ***P < 0.001, t test).*
(G) Representative flow cytometry plots of Granzyme B^+CD8^+ T cells in the IT rMVA-treated tumors from MMTV-PyMT mice.
(H) Percentages of Granzyme B^+ $CD8^+$ T cells in the injected tumors. Data are means ± SD (*n=8; ****P < 0.0001, t test).*
(I) Representative flow cytometry plots of $Foxp3^+CD4^+$ T cells in the injected tumors.
(J) Percentages of $Foxp3^+CD4^+$ T cells in the injected tumors. Data are means ± SD (*n=8; ***P < 0.001, t test).*
(K) Schematic diagram of ex vivo infection of human EMPD tumors with rhMVA.
(L) Percentages of Granzyme B^+CD8^+ T cells and $Foxp3^+CD4^+$ T cells in the rhMVA-treated and non-treated tumor tissues. Data are means ± SD (*n=7; *P < 0.05, **P < 0.01, t test).*

STAR Methods

KEY RESOURCES TABLE

REAGENT or RESOURCE	SOURCE	IDENTIFIER
Antibodies		
BUV395 anti-mouse CD45 (clone 30-F11)	BD	Cat#564279; RRID: AB_2651134
PE/Cy7 anti-mouse CD3 (clone 145-2C11)	BioLegend	Cat#100320; RRID: AB_312685
Pacific Blue anti-mouse CD4 (clone GK1.5)	BioLegend	Cat#100428; RRID: AB_493647
PerCP/Cy5.5 anti-mouse CD8 (clone 53-5.8)	BioLegend	Cat#140418; RRID: AB_2800651
APC anti-mouse Foxp3 (clone 236A/E7)	Thermo Fisher	Cat#17-4777-42; RRID: AB_10804651
PE anti-mouse OX40 (clone OX-86)	BioLegend	Cat#119409; RRID: AB_2272150
Alexa Fluor 647 anti-mouse OX40L (clone RM134L)	BioLegend	Cat#108810; RRID: AB_2207379
BV421 anti-human OX40L (clone iK-1)	BD	Cta#563766; RRID: AB_2738412
Alexa Fluor 488 anti-mouse IFNγ (clone XMG1.2)	BioLegend	Cat#505813; RRID: AB_493312
Alexa Fluor 700 anti-mouse TNFα (clone MP6-XT22)	BioLegend	Cat#506338; RRID: AB_2562918
APC-eFluor 780 anti-mouse CD11b (clone M1/70)	Thermo Fisher	Cat#47-0112-82; RRID: AB_1603193
Alexa Fluor 700 anti-mouse CD11c (clone N418)	BioLegend	Cat#117320; RRID: AB_528736
PerCP/Cyanine5.5 anti-mouse Ly-6G (clone HK1.4)	BioLegend	Cat#128012; RRID: AB_1659241
Brilliant Violet 570 anti-mouse Ly-6G (clone 1A8)	BioLegend	Cat#127629; RRID: AB_10899738
PerCP/Cyanine5.5 anti-mouse F4/80 (cloneBM8)	Thermo Fisher	Cat#45-4801-82; RRID: AB_914345
Brilliant Violet 605 anti-mouse NK1.1 (clone PK136)	BioLegend	Cat#108753; RRID: AB_2686977
Pacific Blue anti-mouse B220 (clone RA3-682)	BioLegend	Cat#103227; RRID: AB_492876
Brilliant Violet 711 anti-mouse CD103 (clone 2E7)	BioLegend	Cat#121435; RRID: AB_2686970
PE anti-mouse CD24 (clone: M1/69)	Thermo Fisher	Cat#12-0242-83; RRID: AB_465603
eFluor450 anti-mouse MHC-II (clone: M5/114.15.2)	Thermo Fisher	Cat#48-5321-80; RRID: AB_1272241
APC/Cyanine7 anti-mouse CD86 (clone: GL-1)	BioLegend	Cat#105030; RRID: AB_2244452
Alexa Fluor 647 Goat anti-mouse IgG	Thermo Fisher	Cat#A21235; RRID: AB_2535804
Mouse anti-human Flt3LG	Thermo Fisher	Cat#MA5-23827, RRID: AB_2608656
PE Texas Red anti-human Granzyme B (clone: GB11)	Thermo Fisher	Cat#GRB17; RRID: AB_2536540

Alexa Fluor 700 anti-human CD45 (clone: HI30)	BioLegend	Cat#304024; RRID: AB_493761
PE/Cyanine7 anti-human CD3 (clone: OKT3)	BioLegend	Cat#317334; RRID: AB_2561452
PerCP/Cyanine5.5 anti-human CD8 (clone: HIT8a)	BioLegend	Cat#300924; RRID: AB_1575074
Pacific Blue anti-human CD4(clone: OKT4)	BioLegend	Cat#317424; RRID: AB_571953
APC anti-human Foxp3 (clone: 236A/E7)	Thermo Fisher	Cat#17-4777-42; RRID: AB_10804651
Alexa Fluor 647 anti-human CD86 (clone: IT2.2)	BioLegend	Cat#305416; RRID: AB_528883
PE Anti-human OX40 (Ber-ACT35)	BioLegend	Cat#350004; RRID: AB_10645478
Anti-mouse CD3ε (clone: 145-2C11)	BioLegend	Cat#100302; RRID: AB_312667
Anti-mouse IFNAR-1 (Clone MAR1-5A3)	Bio X Cell	Cat#BE0241; RRID: AB_2687723
Anti-mouse PD-L1 (Clone 10F.9G2)	Bio X Cell	Cat#BE0101; RRID: AB_10949073
Anti-mouse CD8α (Clone 2.43)	Bio X Cell	Cat#BE0061; RRID: AB_1125541
Anti-mouse CD4 (Clone GK1.5)	Bio X Cell	Cat#BE0003-1; RRID: AB_1107636
Bacterial and Virus Strains		
MVA	provided by G. Sutter (University of Munich)	N/A
MVAΔE5R	This paper	N/A
rMVA	This paper	N/A
rhMVA	This paper	N/A
MVAΔE5R-hFlt3L	This paper	N/A
MVAΔE5R-mOX40L	This paper	N/A
Biological Samples		
Human EMPD samples	Dermatology Service, MSKCC	N/A
Chemicals, Peptides, and Recombinant Proteins		
Eagle's minimal essential medium	Life Technologies	Cat#11095-080
RPMI-1640	Corning	Cat#10-041-CV
Fetal bovine serum	Corning	Cat#35-010-CV
Penicillin/Streptomycin	Corning	Cat#400-109
PBS	Corning	Cat#21-040-CV
EDTA	Invitrogen	Cat#15575-038
ACK lysis buffer	Lonza	Cat#10-548E
Trypsin	Corning	Cat#25-052-CI
PowerUp™SYBR™ Green Master Mix	Thermo Fisher	Cat#A25776
FTY720	Selleckchem	Cat#S5002
Diphtheria toxin	Sigma-Aldrich	Cat#D0564
Liberase™ TL	Roche	Cat#5401020001
Collagenase D	Roche	Cat#11088866001
DNase I	Sigma-Aldrich	Cat#11284932001

CD11c MicroBeads	Miltenyi Biotec	Cat#130-125-835
LIVE/DEAD™ Fixable Aqua Stain	Thermo Fisher	Cat#L34965
Zombie Nir cell viability dye	BioLegend	Cat#423106
CellTrace™ Violet	Thermo Fisher	Cat#C34557
Cell stimulation cocktail	Thermo Fisher	Cat#00-4970-93
recombinant mouse GM-CSF	BioLegend	Cat#576304
recombinant human GM-CSF	PeproTech	Cat#300-03
recombinant human IL-4	PeproTech	Cat#200-04
Puromycin	Sigma	Cat#P9620
Gateway BP Clonase II Enzyme mix	Thermo Fisher	Cat#11789100
Gateway LR Clonase II Enzyme mix	Thermo Fisher	Cat#11791020
One Shot OmniMax 2T1 Chemically Competent	Thermo Fisher	Cat#C854003
Gibson Assembly Master Mix	NEB	Cat#E2600L
NEB 10-beta Competent E. coli	NEB	Cat#E3019I
Critical Commercial Assays		
RNeasy Plus mini kit	Qiagen	Cat#74136
RNeasy Plus micro kit	Qiagen	Cat#74034
cDNA synthesis kit	Thermo Fisher	Cat#AB1453B
Mouse IFNβ ELISA kit	PBL	Cat#42400-1
Foxp3/Transcription factor fixation and permeabilization kit	Thermo Fisher	Cat#00-5523-00
Mouse IFN-γ ELISpot Set	BD Biosciences	Cat#551083
Deposited Data		
Raw data for bulk-tumor RNA-seq		
Processed data for bulk-tumor RNA-seq		
Raw data for Treg RNA-seq		
Processed data for Treg RNA-seq		
Experimental Models: Cell Lines		
BHK-21	ATCC	Cat#CCL-10
B16-F10	I. Fidler (MD Anderson)	
B16-F10-mOX40L	This paper	N/A
B16-F10-hFlt3L	This paper	N/A
A20	ATCC	
SK-MEL-28	MSKCC	
Experimental Models: Organisms/Strains		
Mouse: C57BL/6J	The Jackson Laboratory	stock#000664; RRID: IMSR_JAX:000664
Mouse: BALB/cJ	The Jackson Laboratory	stock#00651
Mouse: cGAS$^{-/-}$ (B6(C)-*Cgas*$^{tm1d(EUCOMM)Hmgu}$/J)	The Jackson Laboratory	RRID: IMSR_JAX:026554
Mouse: STING$^{Gt/Gt}$	(Sauer et al., 2011)	RRID: IMSR_JAX:024101
Mouse: Foxp3^{gfp}		
Mouse: Foxp3^{DTR} (B6.129(Cg)-*Foxp3* $^{tm3(DTR/GFP)Ayr}$/J)	The Jackson Laboratory	Stock#016958
Mouse: STAT2$^{-/-}$ (B6.129-*Stat2*^{tm1Shnd}/J)	The Jackson Laboratory	RRID: IMSR_JAX:023309

Mouse: STAT1$^{-/-}$	(Fontenot et al., 2005)	
Mouse: OX40$^{-/-}$	Jackson laboratory	
Mouse: MMTV-PyMT	Dr. Ming Li	
Oligonucleotides		
Primers for qRT-PCR, see Table S1		N/A
Recombinant DNA		
Plasmid: pUC57-mCherry	This paper	N/A
Plasmid: pUC57-hFlt3L	This paper	N/A
Plasmid: pUC57-mOX40L	This paper	N/A
Plasmid: pUC57-hFlt3L-mOX40L	This paper	N/A
Plasmid: pUC57-hFlt3L-hOX40L	This paper	N/A
Plasmid: pQCXIP-mOX40L	This paper	N/A
Plasmid: pQCXIP-hFlt3l	This paper	N/A
Plasmid: pMD2.G	Addgene	Cat#12259; RRID: Addgene_12259
Plasmid: gag/pol	Addgene	Cat#14887; RRID: Addgene_14887
Plasmid: pQCXIP	Addgene	Cat#17474; RRID: Addgene_17474
Plasmid: pDONR^{TM}221	Thermo Fisher	Cat#12536017
Software and Algorithms		
FlowJo v.10.5.3	BD	RRID: SCR_008520
GraphPad Prism 8	GraphPad	RRID: SCR_002798
bcl2fastq 2.19	Illumina	RRID:SCR_015058
cutadapt (V1.18)	github	RRID:SCR_011841
STAR (V2.5.2)	github	RRID:SCR_004463
Cufflinks (V2.1.1)	github	RRID:SCR_014597
DESeq2	bioconductor	RRID:SCR_015687
GSEA (V4.0.3)	Broad Institute	RRID:SCR_003199
Other		

Resource availability

Lead Contact

Further information and requests for resources and reagents used in this study should be directed to and will be fulfilled by the lead contact and the corresponding author, Liang Deng (dengl@mskcc.org).

Materials availability

The materials used in this study are listed in the Key Resources Table. Materials generated in our laboratory are available upon request.

Data and code availability

The RNA-seq data reported in this study have been deposited in the Gene Expression Omnibus database (GEO) under the accession number GEO: ---. We analyzed the RNA-seq data ---

Materials and Methods

Cell lines

BHK-21 (baby hamster kidney cell, ATCC CCL-10) cells were cultured in Eagle's minimal essential medium containing 10% fetal bovine serum (FBS), 0.1 mM nonessential amino acids, penicillin, and streptomycin. The murine melanoma cell line B16-F10 was originally obtained from I. Fidler (MD Anderson Cancer Center). The A20 B cell lymphoma cell line were obtained from ATCC. Both B16-F10 and A20 were maintained in RPMI-1640 medium supplemented with 10% FBS, 0.05 mM 2-mercaptoethanol, penicillin, and streptomycin.

B16 cell line expressing murine OX40L (mOX40L) or human Flt3l (fFlt3l) were created by transduction into B16 cells with vesicular stomatitis virus (VSV) G protein-pseudotyped murine leukemia viruses (MLV) containing pQCXIP-mOX40L or pQCXIP-fFlt3l. Cells were selected and maintained in growth media including 2 μg/ml puromycin for selection of stably transduced cells.

Viruses

The MVA virus was provided by G. Sutter (University of Munich). MVAΔE5R, MVAΔE5R-hFlt3L, MVAΔE5R-mOX40L, rMVA and rhMVA were generated by transfecting pUC57-based plasmids into BHK-21 cells that were infected with MVA at MOI 0.05. Recombinant viruses

were purified after 4~6 rounds of plaque selection based on the fluorescence marker. Viruses were propagated in BHK-21 cells and purified through a 36% sucrose cushion.

Mice

Female C57BL/6J mice and BALB/cJ between 6 and 10 weeks of age were purchased from the Jackson Laboratory (stock #000664 and stock #000651) were used for the preparation of BMDCs and for *in vivo* experiments. These mice were maintained in the animal facility at the Sloan Kettering Institute. All procedures were performed in strict accordance with the recommendations in the Guide for the Care and Use of Laboratory Animals of the National Institutes of Health. The protocol was approved by the Committee on the Ethics of Animal Experiments of Sloan Kettering Cancer Institute. $STING^{Gt/Gt}$ mice were generated in the laboratory of Dr. Russell Vance (University of California, Berkeley). $Foxp3^{gfp}$ and $Foxp3^{DTR}$ mice were generated in the laboratory of Dr. Alexander Y. Rudensky (Memorial Sloan Kettering Cancer Center). MMTV-PyMT mice were provided by Ming Li (Memorial Sloan Kettering Cancer Center). $cGAS^{-/-}$ mice were generated in Herbert (Skip) Virgin's laboratory (Washington University). $STAT1^{-/-}$, $STAT2^{-/-}$ and $OX40^{-/-}$ were purchased from Jackson Laboratory. $OX40^{-/-}Foxp3^{gfp}$ mice were generated in our lab.

TIL isolation and flow cytometry

For TIL or myeloid cells analysis, tumors were minced prior to incubation with Liberase (1.67 Wünsch U/ml) and DNaseI (0.2 mg/ml) for 30 min at 37°C. Tumors were then homogenized by gentleMACS dissociator and filtered through a 70-μm nylon filter. Cell suspensions were washed and resuspended with complete RPMI. For cytokine production analysis, cells were restimulated with Cell Stimulation Cocktail (Thermo Fisher) and GolgiPlug (BD Biosciences) in complete RPMI for 6 h at 37°C. Cells were incubated with appropriate antibodies for surface labeling for 30 min at 4°C after staining dead cells with LIVE/DEAD™ Fixable Aqua Stain (Thermo Fisher). Cells were fixed and permeabilized using Foxp3 fixation and permeabilization kit (Thermo Fisher) for 1 hour at 4°C and then stained for Granzyme B, Foxp3, IFNγ and TNFα.

To analyze transgene expression, cells were infected with various viruses at a MOI of 10 or mock-infected. At 24 h post infection, cells were collected and the cell viability was determined by labeling with LIVE/DEAD™ Fixable Aqua Stain (Thermo Fisher) 15 min at 4°C. Cells were then

sequentially stained with hFlt3L primary antibody, PE-conjugated goat-anti-mouse IgG antibody and AF647-conjugated anti-mOX40L antibody at 4°C, 15 min for each step.

For dendritic cell maturation assay, cells were infected with virus at a MOI of 10 and collected at 16 h post infection. Then cells were stained with anti-CD86 antibody for surface labeling for 30 min at 4 °C. LIVE/DEAD™ Fixable Aqua Stain (Thermo Fisher) was used to stain dead cells. Cells were analyzed using the BD LSRFortessa flow cytometer (BD Biosciences). Data were analyzed with FlowJo software (Treestar).

RNA isolation and Real-time PCR

For the generation of BMDCs, the bone marrow cells (5 million cells in each 15 cm cell culture dish) were cultured in RPMI-1640 medium supplemented with 10% fetal bovine serum (FBS) in the presence of 30 ng/ml GM-CSF (BioLegend) for 10-12 days.

To generate human monocyte-derived dendritic cells, peripheral blood mononuclear cells (PBMC) were prepared by centrifugation on a Ficoll gradient. Monocytes layer was collected and plated to tissue culture dish. After 1 h, non-adherent cells were washed off. The remaining cells were cultured for 5-7 days in RPMI-1640 supplemented with antibiotics (penicillin and streptomycin) and 10% FCS in the presence of 1000 IU/ml GM-CSF (PeproTech) and 500 IU/ml IL-4 (PeproTech).

Cells were infected with various viruses at a MOI of 10 for 1 hour or mock-infected. The inoculum was removed, and the cells were washed with PBS twice and incubated with fresh medium. RNA was extracted from whole-cell lysates with RNeasy Plus Mini kit (Qiagen) and was reverse-transcribed with cDNA synthesis kit (Thermo Fisher). Real-time PCR was performed in triplicate with SYBR Green PCR Master Mix (Life Technologies) and Applied Biosystems 7500 Real-time PCR Instrument (Life Technologies) using gene-specific primers. Relative expression was normalized to the levels of glyceraldehyde-3-phosphate dehydrogenase (GAPDH). The primer sequences for quantitative real-time PCR are listed in Table S1.

Tumor challenge and treatment

For tumor immune cells analysis, B16-F10 cells were implanted intradermally into right and left flanks of the mice (5×10^5 to the right flank and 2.5×10^5 to the left flank). At 7 to 9 days after

747 implantation, the tumors at the right flank were injected with 4×10^7 PFU of rMVA, MVAΔE5R
748 or PBS twice, 2 or 3 days apart. Tumors, spleens and/or tumor draining lymph nodes were har-
749 vested two days after second injection. In some experiments, 50 μg of αIFNAR-1 antibody
750 (MAR1-5A3, BioXcell) were injected into the tumors together with rMVA.
751
752 For survival experiments, 2×10^5 B16-F10 cells were implanted intradermally into the shaved
753 skin on the right flank of WT C57BL/6J mice or age-matched cGAS$^{-/-}$, STING$^{Gt/Gt}$, STAT2$^{-/-}$,
754 STAT1$^{-/-}$ mice. In some experiments, 2×10^5 A20 cells were implanted intradermally into the
755 right flank of WT BALB/cJ mice. At 6 to 9 days after implantation, tumor sizes were measured
756 and tumors that are 3 mm in diameter or larger were injected with 4×10^7 PFU of rMVA or PBS
757 when the mice were under anesthesia. Viruses were injected twice weekly as specified in each
758 experiment and tumor sizes were measured twice a week. Tumor volumes were calculated ac-
759 cording to the following formula: l (length) × w (width) × h (height)/2. Mice were euthanized for
760 signs of distress or when the diameter of the tumor reached 10 mm. For depletion of T cells, de-
761 pletion antibodies for CD8$^+$ and CD4$^+$ cells (200 μg of clone 2.43 and GK1.5, BioXcell) were
762 injected intraperitoneally twice weekly starting 1 day before viral injection, and they were used
763 until the animals either died, were euthanized, or were completely clear of tumors. In some ex-
764 periments, 25 μg of FTY720 diluted in 100 μl deionized water was injected intraperitoneally
765 twice weekly starting 1 day before viral injection.
766 For depletion of Tregs, 2×10^5 B16-F10 cells were implanted intradermally into the shaved skin
767 on the right flank of Foxp3^{DTR} mice. Diphtheria toxin (DT) were injected were injected intraperi-
768 toneally twice weekly starting 1 day before viral injection, and they were used until the endpoint.
769 In the bilateral tumor implantation model, B16-F10 cells were implanted intradermally into right
770 and left flanks of C57BL/6J mice (5×10^5 to the right flank and 1×10^5 to the left flank). At 7 days
771 after implantation, the tumors at the right flank were injected with 4×10^7 PFU of rMVA or PBS.
772 250μg αPD-L1 antibody (10F.9G2, BioXcell) was injected intraperitoneally twice weekly.
773 For the tumor rechallenge study, the survived mice (more than 40 days after initiation of intra-
774 tumoral virotherapy) were rechallenged with intradermal delivery of a lethal dose of B16-F10
775 (1×10^5 cells) at the contralateral side.
776

ELISpot assay

Spleens were mechanically disrupted by gentleMACS^{TM} dissociator and red blood cells were lysed by ACK lysing buffer. 1×10^6 splenocytes were co-cultured with 2.5×10^5 irradiated B16-F10 in complete RPMI medium overnight. IFNγ^+ splenocytes were detected by Mouse IFNγ ELISPOT kit (BD Biosciences)

In vitro Treg suppression assay

5×10^5 WT B16-F10 cells were implanted intradermally into the right and left flanks of Foxp3^{gfp} and OX40$^{-/-}$Foxp3^{gfp} mice. Tumors and spleens were harvested when tumor sizes reached 5 mm in diameter or larger and processed into single cell suspensions as described above. Cells were stained with anti-CD45.2 (AF700), CD4 (Pacific Blue) and OX40 (PE) antibodies for 30 min at 4 °C. LIVE/DEAD™ Fixable Aqua Stain (Thermo Fisher) was used to stain dead cells. Treg Cells were sorted into CD4$^+$GFP$^+$OX40^{hi} and CD4$^+$GFP$^+$OX40^{lo} populations. Naive CD4$^+$ T Cells were sorted from mouse spleen. Spleens from CD45.1 congenic mouse were harvested, chopped and digested with Collagenase D (2.5 mg/ml) and DNaseI (50 μg/ml) for 30 min at 37°C. CD11c$^+$ DCs were then isolated by CD11c MicroBeads (Miltenyi Biotec). CTV-labeled 4×10^4 native CD4$^+$ T cells were co-cultured with 1×10^5 CD11c$^+$ DCs. Purified CD4$^+$GFP$^+$OX40^{hi}, CD4$^+$GFP$^+$OX40^{lo} or CD4$^+$GFP$^+$OX40$^{-/-}$ cells were seeded in indicated ratios and cultured in complete RPMI supplemented with 1 μg/ml anti-CD3 antibody for 3 days. Cell were then collected and stained with APC anti-CD4 antibody for 30 min at 4 °C after staining dead cells with Zombie Nir. Data were acquired using the BD LSRFortessa flow cytometer (BD Biosciences). Data were analyzed with FlowJo software (Tree Star).

Bulk tumor RNA-seq

5×10^5 WT B16-F10 cells were implanted intradermally into right and left flanks of WT C57BL/6J or age-matched STING$^{Gt/Gt}$ mice. At 7 days after implantation, the tumors were injected with 4×10^7 PFU of rMVA or PBS. Tumors were harvested 1 day after injection and processed into single cell suspension as described previously. RNA was extracted from whole-cell lysates with RNeasy Plus Mini kit (Qiagen, Hilden, Germany) for RNA-seq.

Library prep and sequencing: Following RNA isolation, total RNA integrity was checked using a 2100 Bioanalyzer (Agilent Technologies, Santa Clara, CA). RNA concentrations were measured

using the NanoDrop system (Thermo Fisher Scientific, Inc., Waltham, MA). Preparation of RNA sample library and RNA-seq were performed by the Genomics Core Laboratory at Weill Cornell Medicine. Messenger RNA was prepared using TruSeq Stranded mRNA Sample Library Preparation kit (Illumina, San Diego, CA), according to the manufacturer's instructions. The normalized cDNA libraries were pooled and sequenced on Illumina NovaSeq6000 sequencer with pair-end 50 cycles.

Treg RNA-seq

5×10^5 WT B16-F10 cells were implanted intradermally into right and left flanks of $Foxp3^{GFP}$ mice. When tumor diameter reached 5 mm, mice were euthanized, and tumors and spleens were harvested and processed into single cell suspension as described before. $CD4^+GFP^+OX40^{hi}$ and $CD4^+GFP^+OX40^{low}$ populations from tumors and spleens were purified by FACS sorting. RNA was extracted with RNeasy Plus Micro kit (Qiagen). Following RNA isolation, total RNA integrity was checked using a 2100 Bioanalyzer (Agilent Technologies, Santa Clara, CA). RNA concentrations were measured using the NanoDrop system (Thermo Fisher Scientific, Inc., Waltham, MA). The cDNA synthesis and amplification were performed by SMART-Seq v4 ultra low input RNA kit (Takara Bio USA, Mountain View, CA, USA) starting with less than 1 ng of total RNA from each sample. 150 pg of qualified full-length double strand cDNA was used and processed to Illumina library construction with the Nextera XT DNA Library Preparation Kits (Illumina, San Diego, CA). Then the normalized cDNA libraries were pooled and sequenced on Illumina NovaSeq6000 sequencer with pair-end 50 cycles.

RNA-seq data analysis

The raw sequencing reads in BCL format were processed through bcl2fastq 2.19 (Illumina) for FASTQ conversion and demultiplexing. After trimming the adaptors with cutadapt (version1.18)(https://cutadapt.readthedocs.io/en/v1.18/), RNA reads were aligned and mapped to the GRCh38 human reference genome by STAR (Version2.5.2) (https://github.com/alexdobin/STAR) (Dobin et al., 2013), and transcriptome reconstruction was performed by Cufflinks (Version 2.1.1) (http://cole-trapnell-lab.github.io/cufflinks/). The abundance of transcripts was measured with Cufflinks in Fragments Per Kilobase of exon model per Million mapped reads (FPKM) (Trapnell et al., 2013; Trapnell et al., 2010). Gene expression

839 profiles were constructed for differential expression, cluster, and principle component anal-
840 yses with the DESeq2 package (https://bioconductor.org/packages/re-
841 lease/bioc/html/DESeq2.html) (Love et al., 2014). For differential expression analysis, pairwise
842 comparisons between two or more groups using parametric tests where read-counts follow a neg-
843 ative binomial distribution with a gene-specific dispersion parameter. Corrected p-values were
844 calculated based on the Benjamini-Hochberg method to adjusted for multiple testing.

845 The GSEA analysis was done using GSEA software version 4.0.3 (Subramanian et al., 2005)
846 from the Broad Institute(http://www.gsea-msigdb.org/gsea/index.jsp), which uses predefined
847 gene sets from the Molecular Signatures Database (MSigDB v7.4) (Subramanian et al., 2005).
848 We used the hallmark gene sets collection for the present study. Genes were ranked by the test
849 statistic value obtained from differential expression analysis and the pre-ranked version of the
850 tool was used to identify significantly enriched biological pathways. The minimum and maxi-
851 mum criteria for selection of gene sets from the collection were 15 and 500 genes, respectively.

852 **Human tumor specimens**

853 Fresh biopsy samples from patients with Extramammary Paget's disease were obtained at the
854 dermatology service in the Department of Medicine of Memorial Sloan Kettering Cancer Center.
855 Written informed consents were obtained from patients enrolled in the protocol approved by Me-
856 morial Sloan Kettering Cancer Center Institutional Review Board (IRB). Studies were conducted
857 in accordance with National Institutes of Health and institutional guidelines for human subject
858 research. Tumor tissues were cut into small pieces using a pair of fine scissors. They were in-
859 fected with rhMVA or mock-infected. Cells were collected after 24 h and processed for FACS
860 analyses.
861

862 **Statistical analysis**

863 Two-tailed unpaired Student's t test was used for comparisons of two groups in the studies. Sur-
864 vival data were analyzed by log-rank (Mantel-Cox) test. The p values deemed significant are in-
865 dicated in the figures as follows: *, $p < 0.05$; **, $p < 0.01$; ***, $p < 0.001$; ****, $p < 0.0001$. The
866 numbers of animals included in the study are discussed in each figure legend.
867
868

Acknowledgements

We thank Alexander Y. Rudensky for Foxp3^{gfp} and Foxp3^{DTR} mice. We thank the Flow Cytometry Core Facility and Molecular Cytology Core Facility at the Sloan Kettering Institute and Genomic Resources Core Facility at Weill Cornell Medical College. This work was supported by NIH grants K-08 AI073736 (L.D.), R56AI095692 (L.D.), R03 AR068118 (L.D.), R01 CA56821 (J.D.W). R01 AI091707 (C.M.R.), Charles H. Revson Senior Fellowship in Biomedical Science (J.M.L), a Black Family Metastasis Center Fellowship (J.M.L.), Society of Memorial Sloan Kettering (MSK) research grant (L.D.), MSK Technology Development Fund (L.D.), Parker Institute for Cancer Immunotherapy Career Development Award (L.D.), sponsored research agreement from IMVAQ Therapeutics (L.D.). This work was supported in part by the Swim across America (J.D.W., T.M.), Ludwig Institute for Cancer Research (J.D.W., T.M.), This research was also funded in part through the NIH/NCI Cancer Center Support Grant P30 CA008748.

Author Contributions

Author contributions: N.Y., Y.W. and L.D. were involved in all aspect of this study, including conceiving the project, designing and performing experiments, data analyses and interpretation, and manuscript writing. S.L. assisted some mouse experiments and human tumor ex vivo infection experiments and analyzed the data. G.M, J.W., W.Y. J.C. assisted with construct designs and viral engineering. J.M.L. analyzed RNA-seq data on regulatory T cells. A.Y.T. and T.Z. analyzed the bulk RNA-seq data from tumors. A.R. provided human tumor samples. J.D.W., T.M, C.M.R. and J.Z.X. assisted in experimental design, data interpretation, and manuscript preparation. All authors are involved in manuscript preparation. L.D. provided overall supervision of the study.

Competing interests

Memorial Sloan Kettering Cancer Center filed a patent application for the use of recombinant MVAΔE5R-Flt3L-OX40L as monotherapy or in combination with immune checkpoint blockade for solid tumors. L.D., J.D.W., T.M., N.Y. Y.W. are authors on the patent, which has been licensed to IMVAQ Therapeutics. L.D., J.D.W., T.M., W.Y., J.C., N.Y. are co-founders of IMVAQ Therapeutics and C.M.R. is a member of the scientific advisory board of IMVAQ Therapeutics. T.M. is a consultant of Immunos Therapeutics and Pfizer. He has research support from Bristol Myers Squibb; Surface Oncology; Kyn Therapeutics; Infinity Pharmaceuticals, Inc.;

Peregrine Pharmaceuticals, Inc.; Adaptive Biotechnologies; Leap Therapeutics, Inc.; and Aprea. He has patents on applications related to work on oncolytic viral therapy, alpha virus-based vaccine, neoantigen modeling, CD40, GITR, OX40, PD-1, and CTLA-4. J.D.W. is a consultant for Adaptive Biotech, Advaxis, Am-gen, Apricity, Array BioPharma, Ascentage Pharma, Astellas, Bayer, Beigene, Bristol Myers Squibb, Celgene, Chugai, Elucida, Eli Lilly, F Star, Genentech, Imvaq, Janssen, Kleo Pharma, Linnaeus, MedImmune, Merck, Neon Therapeutics, Ono, Polaris Pharma, Polynoma, Psioxus, Puretech, Recepta, Trieza, Sellas Life Sciences, Serametrix, Surface Oncology, and Syndax. Research support: Bristol Myers Squibb, Medimmune, Merck Pharmaceuticals, and Genentech. Equity: Potenza Therapeutics, Tizona Pharmaceuticals, Adaptive Biotechnologies, Elucida, Imvaq, Beigene, Trieza, and Linnaeus. Honorarium: Esanex. Patents: xenogeneic DNA vaccines, alphavirus replicon particles ex-pressing TRP2, MDSC assay, Newcastle disease viruses for cancer therapy, genomic signature to identify responders to ipilimumab in melanoma, engineered vaccinia viruses for cancer immunotherapy, anti-CD40 agonist monoclonal antibody (mAb) fused to monophosphoryl lipid A (MPL) for cancer therapy, CAR T cells targeting differentiation antigens as means to treat cancer,anti-PD-1 antibody, anti-CTLA-4 antibodies, and anti-GITR antibodies and methods of use thereof.

REFERENCES

Barsheshet, Y., Wildbaum, G., Levy, E., Vitenshtein, A., Akinseye, C., Griggs, J., Lira, S.A., and Karin, N. (2017). CCR8(+)FOXp3(+) Treg cells as master drivers of immune regulation. Proc Natl Acad Sci U S A *114*, 6086-6091.

Bommareddy, P.K., Shettigar, M., and Kaufman, H.L. (2018). Integrating oncolytic viruses in combination cancer immunotherapy. Nat Rev Immunol *18*, 498-513.

Chesney, J., Puzanov, I., Collichio, F., Singh, P., Milhem, M.M., Glaspy, J., Hamid, O., Ross, M., Friedlander, P., Garbe, C.*, et al.* (2018). Randomized, Open-Label Phase II Study Evaluating the Efficacy and Safety of Talimogene Laherparepvec in Combination With Ipilimumab Versus Ipilimumab Alone in Patients With Advanced, Unresectable Melanoma. J Clin Oncol *36*, 1658-1667.

Chinen, T., Kannan, A.K., Levine, A.G., Fan, X., Klein, U., Zheng, Y., Gasteiger, G., Feng, Y., Fontenot, J.D., and Rudensky, A.Y. (2016). An essential role for the IL-2 receptor in Treg cell function. Nat Immunol *17*, 1322-1333.

Coghill, J.M., Fowler, K.A., West, M.L., Fulton, L.M., van Deventer, H., McKinnon, K.P., Vincent, B.G., Lin, K., Panoskaltsis-Mortari, A., Cook, D.N.*, et al.* (2013). CC chemokine receptor 8 potentiates donor Treg survival and is critical for the prevention of murine graft-versus-host disease. Blood *122*, 825-836.

Cohen, A.D., Schaer, D.A., Liu, C., Li, Y., Hirschhorn-Cymmerman, D., Kim, S.C., Diab, A., Rizzuto, G., Duan, F., Perales, M.A.*, et al.* (2010). Agonist anti-GITR monoclonal antibody induces melanoma tumor immunity in mice by altering regulatory T cell stability and intra-tumor accumulation. PLoS One *5*, e10436.

Croft, M. (2009). The role of TNF superfamily members in T-cell function and diseases. Nat Rev Immunol *9*, 271-285.

Croft, M., So, T., Duan, W., and Soroosh, P. (2009). The significance of OX40 and OX40L to T-cell biology and immune disease. Immunol Rev *229*, 173-191.

Dai, P., Wang, W., Cao, H., Avogadri, F., Dai, L., Drexler, I., Joyce, J.A., Li, X.D., Chen, Z., Merghoub, T.*, et al.* (2014). Modified vaccinia virus Ankara triggers type I IFN production in murine conventional dendritic cells via a cGAS/STING-mediated cytosolic DNA-sensing pathway. PLoS Pathog *10*, e1003989.

Dai, P., Wang, W., Yang, N., Serna-Tamayo, C., Ricca, J.M., Zamarin, D., Shuman, S., Merghoub, T., Wolchok, J.D., and Deng, L. (2017). Intratumoral delivery of inactivated modified vaccinia

959 virus Ankara (iMVA) induces systemic antitumor immunity via STING and Batf3-dependent
960 dendritic cells. Sci Immunol *2*.
961
962 Davola, M.E., and Mossman, K.L. (2019). Oncolytic viruses: how "lytic" must they be for
963 therapeutic efficacy? Oncoimmunology *8*, e1581528.
964
965 Deng, L., Liang, H., Xu, M., Yang, X., Burnette, B., Arina, A., Li, X.D., Mauceri, H., Beckett, M.,
966 Darga, T*., et al.* (2014). STING-Dependent Cytosolic DNA Sensing Promotes Radiation-Induced
967 Type I Interferon-Dependent Antitumor Immunity in Immunogenic Tumors. Immunity *41*, 843-
968 852.
969
970 Dobin, A., Davis, C.A., Schlesinger, F., Drenkow, J., Zaleski, C., Jha, S., Batut, P., Chaisson, M.,
971 and Gingeras, T.R. (2013). STAR: ultrafast universal RNA-seq aligner. Bioinformatics *29*, 15-21.
972 Field, C.S., Baixauli, F., Kyle, R.L., Puleston, D.J., Cameron, A.M., Sanin, D.E., Hippen, K.L., Loschi,
973 M., Thangavelu, G., Corrado, M*., et al.* (2020). Mitochondrial Integrity Regulated by Lipid
974 Metabolism Is a Cell-Intrinsic Checkpoint for Treg Suppressive Function. Cell Metab *31*, 422-437
975 e425.
976
977 Gilbert, S.C. (2013). Clinical development of Modified Vaccinia virus Ankara vaccines. Vaccine
978 *31*, 4241-4246.
979
980 He, N., Fan, W., Henriquez, B., Yu, R.T., Atkins, A.R., Liddle, C., Zheng, Y., Downes, M., and
981 Evans, R.M. (2017). Metabolic control of regulatory T cell (Treg) survival and function by Lkb1.
982 Proc Natl Acad Sci U S A *114*, 12542-12547.
983
984 Hirschhorn-Cymerman, D., Budhu, S., Kitano, S., Liu, C., Zhao, F., Zhong, H., Lesokhin, A.M.,
985 Avogadri-Connors, F., Yuan, J., Li, Y*., et al.* (2012). Induction of tumoricidal function in CD4+ T
986 cells is associated with concomitant memory and terminally differentiated phenotype. J Exp
987 Med *209*, 2113-2126.
988
989 Hirschhorn-Cymerman, D., Rizzuto, G.A., Merghoub, T., Cohen, A.D., Avogadri, F., Lesokhin,
990 A.M., Weinberg, A.D., Wolchok, J.D., and Houghton, A.N. (2009). OX40 engagement and
991 chemotherapy combination provides potent antitumor immunity with concomitant regulatory T
992 cell apoptosis. J Exp Med *206*, 1103-1116.
993
994 Kohlmeier, J.E., Cookenham, T., Roberts, A.D., Miller, S.C., and Woodland, D.L. (2010). Type I
995 interferons regulate cytolytic activity of memory CD8(+) T cells in the lung airways during
996 respiratory virus challenge. Immunity *33*, 96-105.
997
998 Lemos de Matos, A., Franco, L.S., and McFadden, G. (2020). Oncolytic Viruses and the Immune
999 System: The Dynamic Duo. Mol Ther Methods Clin Dev *17*, 349-358.
1000
1001 Leone, R.D., Sun, I.M., Oh, M.H., Sun, I.H., Wen, J., Englert, J., and Powell, J.D. (2018). Inhibition
1002 of the adenosine A2a receptor modulates expression of T cell coinhibitory receptors and

improves effector function for enhanced checkpoint blockade and ACT in murine cancer models. Cancer Immunol Immunother *67*, 1271-1284.

Liu, K., and Nussenzweig, M.C. (2010). Origin and development of dendritic cells. Immunol Rev *234*, 45-54.

Liu, R., Americo, J.L., Cotter, C.A., Earl, P.L., Erez, N., Peng, C., and Moss, B. (2021). One or two injections of MVA-vectored vaccine shields hACE2 transgenic mice from SARS-CoV-2 upper and lower respiratory tract infection. Proc Natl Acad Sci U S A *118*.

Love, M.I., Huber, W., and Anders, S. (2014). Moderated estimation of fold change and dispersion for RNA-seq data with DESeq2. Genome Biol *15*, 550.

Maj, T., Wang, W., Crespo, J., Zhang, H., Wang, W., Wei, S., Zhao, L., Vatan, L., Shao, I., Szeliga, W.*, et al.* (2017). Oxidative stress controls regulatory T cell apoptosis and suppressor activity and PD-L1-blockade resistance in tumor. Nat Immunol *18*, 1332-1341.

Marabelle, A., Kohrt, H., Sagiv-Barfi, I., Ajami, B., Axtell, R.C., Zhou, G., Rajapaksa, R., Green, M.R., Torchia, J., Brody, J.*, et al.* (2013). Depleting tumor-specific Tregs at a single site eradicates disseminated tumors. J Clin Invest *123*, 2447-2463.

Messenheimer, D.J., Jensen, S.M., Afentoulis, M.E., Wegmann, K.W., Feng, Z., Friedman, D.J., Gough, M.J., Urba, W.J., and Fox, B.A. (2017). Timing of PD-1 Blockade Is Critical to Effective Combination Immunotherapy with Anti-OX40. Clin Cancer Res *23*, 6165-6177.

Murata, K., Ishii, N., Takano, H., Miura, S., Ndhlovu, L.C., Nose, M., Noda, T., and Sugamura, K. (2000). Impairment of antigen-presenting cell function in mice lacking expression of OX40 ligand. J Exp Med *191*, 365-374.

Plitas, G., Konopacki, C., Wu, K., Bos, P.D., Morrow, M., Putintseva, E.V., Chudakov, D.M., and Rudensky, A.Y. (2016). Regulatory T Cells Exhibit Distinct Features in Human Breast Cancer. Immunity *45*, 1122-1134.

Ribas, A., Dummer, R., Puzanov, I., VanderWalde, A., Andtbacka, R.H.I., Michielin, O., Olszanski, A.J., Malvehy, J., Cebon, J., Fernandez, E.*, et al.* (2018). Oncolytic Virotherapy Promotes Intratumoral T Cell Infiltration and Improves Anti-PD-1 Immunotherapy. Cell *174*, 1031-1032.
Ribas, A., and Wolchok, J.D. (2018). Cancer immunotherapy using checkpoint blockade. Science *359*, 1350-1355.

Russell, S.J., Peng, K.W., and Bell, J.C. (2012). Oncolytic virotherapy. Nat Biotechnol *30*, 658-670.

Sauer, J.D., Sotelo-Troha, K., von Moltke, J., Monroe, K.M., Rae, C.S., Brubaker, S.W., Hyodo, M., Hayakawa, Y., Woodward, J.J., Portnoy, D.A.*, et al.* (2011). The N-ethyl-N-nitrosourea-induced

1046 Goldenticket mouse mutant reveals an essential function of Sting in the in vivo interferon
1047 response to Listeria monocytogenes and cyclic dinucleotides. Infect Immun *79*, 688-694.
1048
1049 Schreiber, R.D., Old, L.J., and Smyth, M.J. (2011). Cancer immunoediting: integrating immunity's
1050 roles in cancer suppression and promotion. Science *331*, 1565-1570.
1051
1052 Shrimali, R.K., Ahmad, S., Verma, V., Zeng, P., Ananth, S., Gaur, P., Gittelman, R.M., Yusko, E.,
1053 Sanders, C., Robins, H.*, et al.* (2017). Concurrent PD-1 Blockade Negates the Effects of OX40
1054 Agonist Antibody in Combination Immunotherapy through Inducing T-cell Apoptosis. Cancer
1055 Immunol Res *5*, 755-766.
1056
1057 Subramanian, A., Tamayo, P., Mootha, V.K., Mukherjee, S., Ebert, B.L., Gillette, M.A., Paulovich,
1058 A., Pomeroy, S.L., Golub, T.R., Lander, E.S.*, et al.* (2005). Gene set enrichment analysis: a
1059 knowledge-based approach for interpreting genome-wide expression profiles. Proc Natl Acad
1060 Sci U S A *102*, 15545-15550.
1061
1062 Trapnell, C., Hendrickson, D.G., Sauvageau, M., Goff, L., Rinn, J.L., and Pachter, L. (2013).
1063 Differential analysis of gene regulation at transcript resolution with RNA-seq. Nat Biotechnol
1064 *31*, 46-53.
1065
1066 Trapnell, C., Williams, B.A., Pertea, G., Mortazavi, A., Kwan, G., van Baren, M.J., Salzberg, S.L.,
1067 Wold, B.J., and Pachter, L. (2010). Transcript assembly and quantification by RNA-Seq reveals
1068 unannotated transcripts and isoform switching during cell differentiation. Nat Biotechnol *28*,
1069 511-515.
1070
1071 Villarreal, D.O., L'Huillier, A., Armington, S., Mottershead, C., Filippova, E.V., Coder, B.D., Petit,
1072 R.G., and Princiotta, M.F. (2018). Targeting CCR8 Induces Protective Antitumor Immunity and
1073 Enhances Vaccine-Induced Responses in Colon Cancer. Cancer Res *78*, 5340-5348.
1074
1075 Volz, A., and Sutter, G. (2017). Modified Vaccinia Virus Ankara: History, Value in Basic Research,
1076 and Current Perspectives for Vaccine Development. Adv Virus Res *97*, 187-243.
1077
1078 Wang, W., Liu, S., Dai, P., Yang, N., Wang, Y., Giese, R.A., Merghoub, T., Wolchok, J., and Deng,
1079 L. (2021). Elucidating mechanisms of antitumor immunity mediated by live oncolytic vaccinia
1080 and heat-inactivated vaccinia. J Immunother Cancer *9*.
1081
1082 Wei, S.C., Duffy, C.R., and Allison, J.P. (2018). Fundamental Mechanisms of Immune Checkpoint
1083 Blockade Therapy. Cancer Discov *8*, 1069-1086.
1084
1085 Weinberg, S.E., Singer, B.D., Steinert, E.M., Martinez, C.A., Mehta, M.M., Martinez-Reyes, I.,
1086 Gao, P., Helmin, K.A., Abdala-Valencia, H., Sena, L.A.*, et al.* (2019). Mitochondrial complex III is
1087 essential for suppressive function of regulatory T cells. Nature *565*, 495-499.

Wing, K., Onishi, Y., Prieto-Martin, P., Yamaguchi, T., Miyara, M., Fehervari, Z., Nomura, T., and Sakaguchi, S. (2008). CTLA-4 control over Foxp3+ regulatory T cell function. Science *322*, 271-275.

Woo, S.R., Fuertes, M.B., Corrales, L., Spranger, S., Furdyna, M.J., Leung, M.Y., Duggan, R., Wang, Y., Barber, G.N., Fitzgerald, K.A.*, et al.* (2014). STING-dependent cytosolic DNA sensing mediates innate immune recognition of immunogenic tumors. Immunity *41*, 830-842.

Workenhe, S.T., and Mossman, K.L. (2014). Oncolytic virotherapy and immunogenic cancer cell death: sharpening the sword for improved cancer treatment strategies. Mol Ther *22*, 251-256.

Zamarin, D., Holmgaard, R.B., Subudhi, S.K., Park, J.S., Mansour, M., Palese, P., Merghoub, T., Wolchok, J.D., and Allison, J.P. (2014). Localized oncolytic virotherapy overcomes systemic tumor resistance to immune checkpoint blockade immunotherapy. Sci Transl Med *6*, 226ra232.

Zappasodi, R., Serganova, I., Cohen, I.J., Maeda, M., Shindo, M., Senbabaoglu, Y., Watson, M.J., Leftin, A., Maniyar, R., Verma, S.*, et al.* (2021). CTLA-4 blockade drives loss of Treg stability in glycolysis-low tumours. Nature *591*, 652-658.

Zappasodi, R., Sirard, C., Li, Y., Budhu, S., Abu-Akeel, M., Liu, C., Yang, X., Zhong, H., Newman, W., Qi, J.*, et al.* (2019). Rational design of anti-GITR-based combination immunotherapy. Nat Med *25*, 759-766.

Zaretsky, J.M., Garcia-Diaz, A., Shin, D.S., Escuin-Ordinas, H., Hugo, W., Hu-Lieskovan, S., Torrejon, D.Y., Abril-Rodriguez, G., Sandoval, S., Barthly, L.*, et al.* (2016). Mutations Associated with Acquired Resistance to PD-1 Blockade in Melanoma. N Engl J Med *375*, 819-829.

Zou, W., Wolchok, J.D., and Chen, L. (2016). PD-L1 (B7-H1) and PD-1 pathway blockade for cancer therapy: Mechanisms, response biomarkers, and combinations. Sci Transl Med *8*, 328rv324.

Yang, N., et al., Vaccinia E5 is a major inhibitor of the DNA sensor cGAS. BioRxiv https://doi.org/10.1101/2021.10.25.465197.